Detection of tectonometamorphic discontinuities within the Himalayan orogen: Structural and petrological constraints from the Rasuwa district, central Nepal Himalaya

Fast detection of tectonometamorphic discontinuities within the Himalayan orogen: structural and petrological constraints from Rasuwa District, Central Nepal Himalaya

GIULIA RAPA[1] , PIETRO MOSCA[2] , CHIARA GROPPO[1,2] , FRANCO ROLFO[1,2]

[1]Department of Earth Sciences, University of Torino, Via Valperga Caluso 35, 10125 Turin, Italy

(corresponding author: giulia.rapa@unito.it)

[2] Institute of Geosciences and Earth Resources - National Research Council of Italy (CNR), Via Valperga Caluso 35, 10125 Turin, Italy

Abstract

A detailed structural, lithological and petrological study of different transects in the Rasuwa district of central Nepal Himalaya allows the characterization of the tectonostratigraphic architecture of the area. It also facilitates constraining the P-T evolution of the different units within the Lesser (LHS) and Greater (GHS) Himalayan Sequences. Peak *P–T* conditions obtained for the studied metapelite samples using the pseudosection approach and the Average PT method highlight the existence of four different T/P ratio populations in different tectonometamorphic units: 80 ± 11 °C/kbar (LHS), 66 ± 7 °C/kbar (Ramgarh Thrust Sheet: LHS-Ramgarh Thrust Sheet), 73 ± 1 °C/kbar (Lower-GHS) and 101 ± 12 °C/kbar (Upper-GHS). Integration of structural and petrological data emphasizes the existence of three tectonometamorphic discontinuities bounding these units, characterized by top-to-the-south sense of shear: the Ramgarh Thrust, which separates the LHS (peak metamorphism at ~600 °C, 7.5 kbar) from the overlying LHS-Ramgarh Thrust Sheet (peak metamorphism at ~635 °C, 10 kbar); the Main Central Thrust, which separates the LHS-Ramgarh Thrust Sheet from the Lower-GHS (peak at 700-740 °C, 9.5-10.5 kbar with a prograde increase in both P and T in the kyanite stability field), and the Langtang Thrust, which juxtaposes the Upper-GHS (peak at 780-800°C, 7.5-8.0 kbar with a nearly isobaric heating in the sillimanite stability field) onto the Lower-GHS. An increase in the intensity of deformation, with development of pervasive mylonitic fabrics and/or shear zones, is generally observed approaching the discontinuities from either side.

Overall, data and results presented in this paper demonstrate that petrological and structural analysis combined together, are reliable methods adequate to rapidly

identify tectonometamorphic discontinuities in both the LHS and GHS. Geochronological data from the literature allow the interpretation of these discontinuities as in-sequence thrusts.

Keywords

Himalaya; pseudosection; AvPT method; structural data; tectonometamorphic discontinuity.

1. INTRODUCTION

In the last few years, discoveries of tectonometamorphic discontinuities within the exhumed metamorphic core of the Himalayas (e.g. Larson et al., 2015; Montomoli et al., 2015 and references therein) marked the beginning of a new exciting frontier of research devoted to the understanding of the internal structure of the Himalayan orogen. These discontinuities, mostly interpreted as in-sequence thrusts, especially in western-central Nepal, separate rock packages characterized by different lithological associations, different geochemical features (e.g. Nd isotopes), different metamorphic evolutions and/or different peak metamorphic ages. Over the years, different criteria have been used to identify such discontinuities, including lithological (e.g. Gansser, 1983; Daniel et al. 2003), structural (e.g. Macfarlane et al., 1992; Reddy et al., 1993; Takagi et al., 2003; Law et al., 2004; Martin et al. 2005; Jessup et al., 2006; Searle et al., 2008; Yakymchuk and Godin, 2012; Larson et al. 2013; Larson and Cottle, 2014), geochemical (e.g. Robinson et al. 2001; Martin et al. 2005; Richards et al. 2005), petrological (e.g. Macfarlane, 1995; Fraser et al., 2000; Kohn et al., 2004; Goscombe et al., 2006; Kohn, 2008; Groppo et al., 2009; Imayama et al., 2010; Mosca et al., 2012; Yakymchuk and Godin, 2012; Larson et al. 2013; Wang et al., 2013, 2016; Rolfo et al., 2015; Rapa et al., 2016; Iaccarino et al., 2017) and geochronological (e.g. Harrison et al. 1997; Catlos et al. 2001, 2002; Kohn et al., 2004, 2005; Carosi et al., 2007, 2010; Kohn, 2008; Imayama et al., 2012; Larson et al. 2013; Montomoli et al., 2013; Rubatto et al., 2013; Larson and Cottle, 2014; Ambrose et al., 2015; Iaccarino et al., 2016) criteria.

The Rasuwa Disctrict of central Nepal Himalaya is an ideal natural laboratory for investigating the internal structure of both the Lesser Himalayan Sequence (LHS)

and Greater Himalayan Sequence (GHS) (Fig. 1). Because it offers both a complete cross-section through the LHS and GHS, and is easily accessible, different portions of this region have been investigated in detail since the ’90s (e.g. Inger and Harris, 1992; Macfarlane et al., 1992; Macfarlane, 1993, 1995; Upreti, 1999; Fraser et al., 2000; Kohn et al., 2004, 2005; Pearson and DeCelles, 2005; Kohn, 2008). It is not by chance that the first discontinuity within the GHS was identified in this region (Inger and Harris, 1992). In the following decades, other authors focused their attention on the Langtang region and recognized a number of major tectonometamorphic discontinuities within the GHS, using either petrological (e.g. Macfarlane, 1995; Fraser et al., 2000) or structural (Macfarlane et al., 1992; Reddy et al., 1993) evidences. More recently, Kohn et al. (2004, 2005) and Kohn (2004, 2008) combined P–T estimates with geochronological data, to infer the existence of major structures within the GHS (Langtang Thrust) and the LHS (Ramgarh Thrust or Munsiari Thrust), which separate the GHS and LHS in two sub-units, characterized by different peak P–T conditions and by different P–T–t paths.

Although the tectonometamorphic architecture of Langtang is relatively well-known, a combined structural and petrological study of both the LHS and GHS in this region is lacking. Moreover, most of the petrological studies published so far on the Langtang transect, constrained the peak P-T conditions experienced by the different LHS and GHS units, but did not provide information about their P-T paths or evolution. This study aims to fill this knowledge gap. We present new detailed structural, lithological and petrological data for the Langtang transect and for the adjacent western sector towards the village of Gatlang (Fig. 2). These new data, combined with those already published by Rapa et al. (2016) for the nearby Gosainkund-Helambu region, allow us

to fully characterize the tectonostratigraphic architecture of the area, and to constrain the P-T evolution of the different units within the LHS and the GHS.

2. GEOLOGICAL SETTING

The Himalayan orogen derives from the continued collision of the Indian and Eurasian plates, which began at ca. 50 Ma. Its present structure is characterized by four tectonostratigraphic units that extend longitudinally for more than 2000km and are bounded by crustal-scale north-dipping faults (Fig 1).

The uppermost unit is the Tethyan Sedimentary Sequence (TSS: e.g. Gaetani and Garzanti, 1991), separated from the subjacent Greater Himalayan Sequence (GHS) by the South Tibetan Detachment System (STDS).

The Greater Himalayan Sequence (GHS) represents the exhumed metamorphic core of the Himalaya and consists of several km thick sequence of medium-grade to anatectic rocks bounded at its top by the STDS and at its base by the Main Central Thrust (MCT). At least two main domains can be broadly identified within the GHS, characterized by rocks which experienced different metamorphic evolutions (i.e. different P-T paths: e.g. Larson et al., 2010; Mosca et al., 2012; Montomoli et al., 2015 and references therein; Rapa et al., 2016). The lower structural levels of the GHS (Lower-GHS) are medium- to high grade metasediments and granitic orthogneisses, recording a metamorphic grade that increases structurally upward from the garnet and staurolite zones to the sillimanite zone and, locally, to anatexis (e.g. Goscombe et al., 2006; Groppo et al., 2009, 2010; Mosca et al., 2012). The upper GHS (Upper-GHS), roughly corresponds to the Higher Himalayan Crystallines (Pognante and Benna, 1993; Lombardo et al., 1993) and consists of high-grade, often migmatitic, para- and orthogneisses. The Upper-GHS rocks often host dyke

networks and lens-shaped bodies of two-mica and tourmaline-bearing leucogranites, characterized by a progressive decrease in peak-pressure structurally up section (Lombardo et al., 1993; Pognante and Benna, 1993; Davidson et al., 1997; Guillot, 1999; Hodges, 2000; Groppo et al., 2012, 2013).

The underlying Lesser Himalayan Sequence (LHS) consists of low-grade metasediments (metapelitic schists, impure marbles, calcschists and quartzites) associated with granitic orthogneiss. To the south, the LHS lithologies are juxtaposed with the molassic sediments of the Siwalik foreland across the Main Boundary Thrust (MBT, Fig. 1). Numerous stratigraphic classifications have been proposed for the LHS across the Himalaya, and correlations through different regions are not straightforward (e.g. Upreti, 1999; McQuarrie et al., 2008, Kohn et al., 2010 and references therein).

In the Gatlang-Langtang and Gosainkund-Helambu regions investigated in this study (Fig. 1), the main tectonic structures bounding these units are the Ramgarh Thrust, the Main Central Thrust and the Langtang Thrust. The Main Central Thrust (MCT) was one of the first crustal-scale tectonic discontinuities described in the Himalaya. This is a large thrust-sense shear zone (MCTZ, Main Central Thrust Zone), ranging in thickness from several hundreds of metres to several kilometres, which emplaces the medium- to high-grade Lower-GHS over the low-grade LHS. The MCT has been mapped across the Himalaya using a variety of different criteria (see Searle et al., 2008 and Martin, 2017 for a review), and despite being the subject of numerous studies over the last few decades, it remains one of the most debated tectonic features of the Himalaya. In central Nepal movement along it has been dated at 24-18 Ma (Godin et al., 2006 for a review). In the Gatlang-Langtang and Gosainkund-Helambu areas, the MCTZ was first mapped by Arita et al. (1973) as a structural

discordance at the base of the GHS anatectic rocks. McFarlane (1992) located the MCTZ between the LHS (mainly pelitic and graphitic schists of the Dunche schists formation) and the GHS (Gosaikunda anatectic gneiss), and she described it as an imbricate shear zone consisting of different lithological units of both LHS and GHS affinity, separated by brittle faults. Later on, Takagi et al. (2003) subdivided the MCTZ into three units involving lithologies from the upper LHS and the lower part of GHS, and emphasized the occurrence of a late top-to-the-north extensional movement along the MCTZ itself.

The Ramgarh Thrust was first identified in the Langtang region by Pearson and DeCelles (2005), combining stratigraphic relationships and Nd isotopic analysis. The Ramgarh Thrust is a discrete tectonostratigraphic boundary located within the LHS (i.e. below the MCTZ), and places the Robang Formation (~1940 Ma according to Pearson & DeCelles, 2005), including also Lower Proterozoic augen gneisses (Ulleri gneiss) and quartzites, above the younger Kuncha Formation (~1860 Ma; e.g. Schelling, 1992; DeCelles et al., 2001; Robinson et al., 2001; Pearson, 2002; Pearson & DeCelles, 2005).

The Langtang Thrust was first identified in the Langtang region by Kohn et al. (2004, 2005) basing on metamorphic and geochronological criteria, although prior to these studies, other authors already described the existence of a major discontinuity within the GHS in the region (Inger and Harris, 1992; Macfarlane, 1995; Fraser et al., 2000). The Langtang Thrust is mainly a metamorphic discontinuity that separates a lower GHS unit (Lower-GHS), characterized by higher pressure at peak–T conditions, from an upper GHS unit (Upper-GHS), which experienced lower pressure at peak–T conditions (e.g. Kohn, 2008).

3. METHODS

3.1 Fieldwork

A detailed geological study combined with mesostructural observations was conducted in central Nepal Himalaya along three transects, crossing both the LHS and the GHS exposed in the Gatlang, Langtang and Gosainkund-Helambu regions (Fig. 1 and 2). A geological map as well as stereo plots of structural elements are shown in Fig. 2. Representative photos of lithologies and meso-structures are given in Figs. 3-7.

3.2 Petrography and mineral chemistry

A total of 184 thin sections were petrographically characterized. Detailed petrologic study was performed on a total of 14 metapelite samples: five from the Gatlang transect (samples 15-19, 14-27a, 15-28b, 15-26b and 15-38), five from the Langtang transect (samples 14-03, 14-25b, 14-24, 14-08a and 14-12) and four from the Gosainkund-Helambu transect (samples 14-44a, 14-61b, 14-71 and 14-52). Nine of these samples have been already described and petrologically modelled using the pseudosection approach by Rapa et al. (2016). Those samples are not described in detail in Section 4.2, but their microstructures are relevant to this study and are summarized in Table 1. Petrographic and mineral chemical features are described in detail for samples 15-19, 15-28b, 15-26b, 15-38 and 14-12.

The rock-forming minerals were analyzed with either a Cambridge Stereoscan 360 (analyses performed prior to 2016) or a Jeol JSM-IT300LV (analyses performed since 2016) Scanning Electron Microscope at the Department of Earth Sciences, University of Torino. Both the instruments were equipped with an energy dispersive spectrometry (EDS) Energy 200 system and an SDD X-Act3 detector (Oxford Inca

192 Energy). The operating conditions were 50 s counting time and 15 kV accelerating
193 voltage. SEM-EDS quantitative data (spot size 2 μm) were acquired and processed
194 using the Microanalysis Suite Issue 12, INCA Suite version 4.01; natural mineral
195 standards were used to calibrate the raw data; the $\phi\rho Z$ correction (Pouchou and
196 Pichoir, 1988) was applied. Table 2 summarizes the representative chemical
197 compositions for the main minerals in each sample. Mineral abbreviations are
198 according to Whitney and Evans (2010). Representative photos of microstructures
199 are presented in Fig. 8.
200
201 **3.3 Optimal thermobarometry**
202 The Thermocalc "Average PT" (AvPT) method (i.e. "Optimal thermobarometry":
203 Powell and Holland, 1994) was applied to all of the samples in this study including
204 the 9 samples already investigated using the P-T pseudosection approach by Rapa
205 et al., (2016). Thermocalc v3.33 (Powell and Holland, 1994) and the Holland and
206 Powell (1998, revised in 2004) dataset were used. Activity-composition relationships
207 were calculated using the software AX. The internal consistency of the method was
208 examined with the samples additionally investigated using the pseudosection
209 approach (both in this paper and in Rapa et al., 2016). To maintain the consistency
210 between the thermodynamic datasets used for pseudosections and AvPT, we chose
211 not to use the updated version of the dataset (version 6.02) based on Holland and
212 Powell (2011).
213 The AvPT method evaluates P-T conditions through the calculation of a set of
214 independent reactions representing all the equilibria between the end-members of
215 the equilibrium assemblage; if the number of reactions between end-members is too
216 low, the method does not converge to a result. Mineral compositions used for

thermobarometric calculations are given in Tables S1a-e, and results in Table 3. For samples with zoned garnets, calculations were done considering garnet core and garnet rim compositions, combined with the mineral assemblages in equilibrium with each of them. The presence of melt in equilibrium with the peak mineral assemblage in some samples was simulated by reducing the activity of H_2O ($0.7<aH_2O<1$) (see Mosca et al., 2012), because it is not possible to include the melt solution model in AvPT calculations.

3.4 Pseudosection modelling

One sample (15-26b) out of the 14 samples investigated in this study has been modelled using the pseudosection approach in the system MnNCKFMASTH; Fe^{3+} was neglected because Fe^{3+}-rich oxides are absent and the amount of Fe^{3+} in the analyzed minerals is very low. Pseudosections for nine additional samples have been already calculated and discussed in detail by Rapa et al. (2016).

Pseudosections were calculated using Perplex 6.7.2 (version June 2015; Connolly, 1990, 2009) and the internally consistent thermodynamic dataset and equation of state for H_2O of Holland and Powell (1998, revised 2004). The minerals considered in the calculation were: garnet, biotite, chlorite, kyanite, andalusite, sillimanite, staurolite, zoisite/clinozoisite, plagioclase, white mica, K-feldspar, cordierite, quartz, titanite, rutile, ilmenite, in addition to melt. The following solution models were used: garnet, chloritoid, cordierite and staurolite (Holland and Powell, 1998), biotite (Tajčmanová et al., 2009), chlorite (Holland et al., 1998), plagioclase (Newton et al., 1980), white mica (Coggon and Holland 2002; Auzanneau et al., 2010), K-feldspar (Thompson and Hovis, 1979), and melt (Holland and Powell, 2001; White et al., 2001, 2007). The fluid was considered as pure H_2O ($aH_2O=1$).

242

243 # 4. RESULTS

244

245 ## 4.1 Tectonostratigraphy of the Gatlang, Langtang, and Gosainkund-Helambu
246 ## regions

247 Along the Gatlang, Langtang and Gosainkund-Helambu transects, both the LHS and
248 the GHS tectonostratigraphic units are exposed, the latter being subdivided into the
249 Lower-GHS and the Upper-GHS.

250

251 ### *4.1.1 Lesser Himalayan Sequence*

252 *Lithostratigraphic features*

253 The LHS is exposed in the westernmost part of the study area, south of the village of
254 Syabrubensi, and it extends northward up to Tatopani (Fig. 2). In its structurally lower
255 levels, the LHS is mainly composed of grey to pale-green, fine-grained phyllites,
256 slates and phyllitic schists (Fig. 3a,b), with ubiquitous dm-thick intercalations of
257 metasandstones characterized by the occurrence of detrital grains of quartz, feldspar
258 and tourmaline. The gradual increase of metamorphic grade up-section (i.e. from SW
259 to NE) is already evident at the outcrop scale and is evidenced by the occurrence of
260 Chl + Wm assemblages at the lowest structural levels, passing to two-mica (±Grt ±St
261 ±Ky) assemblages close to the MCT. In its uppermost structural levels, the LHS is
262 more heterogeneous, with several carbonatic and graphitic units intercalated with the
263 phyllites. Specifically, the most common lithologies include: (i) laminated impure
264 marbles, calcareous phyllites and calcschists, and (ii) dm-thick layers of graphitic
265 schists. The bedding in the marbles is mm- to pluri-cm thick, and the foliation is
266 defined by the preferred orientation of Wm ± Phl ± Chl ± Amph. Calcareous phyllites

and calcschists occur as dm–thick layers and contain Wm ± Bt ± Phl ± Chl ± Gr in varying proportions.

The dominantly phyllitic lithologies with quarzitic intercalations exposed at the lowermost structural levels of the LHS can be ascribed to the Lower-LHS according to the definition of Kohn et al. (2010) (also known as Kuncha and Ranimata Formations in central and western Nepal, respectively; Stöcklin, 1980; Person and DeCelles, 2005; Robinson et al., 2006); the abundant carbonatic and graphitic rocks can be ascribed to the Upper-LHS (Kohn et al., 2010).

Upward in the sequence, the dominantly carbonatic and graphitic lithologies give way to strongly foliated phyllitic schists with abundant intercalations of Wm ± Bt ± Chl ± St banded quartzite (Fig. 3c,d), and by two-mica mylonitic orthogneisses forming a decametric-thick body thinning towards SE (Fig. 3e,f). Pearson and DeCelles (2005) ascribed the quartzites and phyllitic schists to the Kushma and Robang Formations, respectively, which represent the lowermost Paleoproterozoic levels of the LHS. The mylonitic augen-gneiss may be correlated to the Ulleri gneiss (e.g. Le Fort and Rai, 1999), stratigraphically intercalated within the lowermost portion of the Kuncha-Ranimata Formations in the Lower-LHS. This suggests that, in the study area, Lower-LHS lithologies (i.e. quartzites: Robang-Kushma Fm.; augen gneisses: Ulleri gneiss) are tectonically emplaced over Upper-LHS lithologies (i.e. calcschists and marbles). The thrust fault responsible for this emplacement, the Ramgarh Thrust, has been documented by a number of authors (e.g. Schelling, 1992; DeCelles et al., 2001; Robinson et al., 2001; Pearson, 2002; Kohn et al., 2004) basing on stratigraphic, geochemical (Nd isotopic analysis) and geochronological data. In the following, the relatively thin package of Lower-LHS lithologies bounded by the Ramgarh Thrust at

its bottom and by the MCT at its top, will be referred to as LHS-Ramgarh Thrust Sheet.

Structural features

The main pervasive foliation in the LHS is represented by the $S_{2(LHS)}$, which resulted from a ductile $D_{2(LHS)}$ deformation event intensively transposing earlier planar elements (i.e. bedding and an early $S_{1(LHS)}$ foliation). At the outcrop scale, planar elements can, therefore, be generally described as a S_2-$S_{1(LHS)}$ composite foliation (Figs. 3a,e and Fig. 4a,b).

In the phyllites, the $S_{2(LHS)}$ is defined by Wm ± Chl ± Bt; the rim of porphyroblastic garnet is locally in equilibrium with this foliation. The $S_{2(LHS)}$ transposed an early $S_{1(LHS)}$ foliation defined by Wm ± Chl ± Bt, locally preserved in microlithons as well as an internal foliation (Chl + Ilm ± Gr) in garnet porphyroblasts (Fig. 3b). Syntectonic quartz veins are often stretched and boudinated along the $S_{2(LHS)}$. In marbles, the $S_{2(LHS)}$ is roughly parallel to a mm- to cm- thick compositional bedding, and it is marked by the preferred orientation of Wm ± Phl ± Chl ± Amph. In a few quartzite outcrops, the dominant $S_{2(LHS)}$ is at high angle with respect to an original compositional banding. In the augen-gneisses, the $S_{2(LHS)}$ manifests as a mylonitic foliation defined by Bt + Wm layers wrapping around rotated Kfs ± Pl porphyroclasts (Fig. 3f). The aplites intercalated within the augen-gneisses are mostly transposed in the $S_{2(LHS)}$ foliation.

The $S_{2(LHS)}$ dips, on average, to the NNE in the northern sectors of the study area and progressively rotates towards NE-ENE moving to the east. It contains a $L_{2(LHS)}$ stretching lineation (defined by elongated Kfs porphyroclasts and minerals) plunging between N and NE. $F_{2(LHS)}$ folds (whose axial plane is approximated by the $S_{2(LHS)}$)

316 have stretched limbs and slightly thickened hinges, and often have an asymmetric
317 shape, synthetic with top-to-the-south shearing. The relationships between $L_{2(LHS)}$ and
318 $F_{2(LHS)}$ axes suggest non-cylindrical folding. The abundant kinematic indicators (e.g.
319 mica-fish, rotated clasts, S-C shear cleavages, asymmetry of stretched Qz lenses) at
320 outcrop and microscope scale indicate a consistent top-to-the-south-southwest sense
321 of shear (Fig. 4a,b). $S_{2(LHS)}$ and C-surfaces intersect on average between 30° and
322 10°.
323 Mesoscopic shear zones (from cm- to metre-thick) related to the $D_{2(LHS)}$ event can be
324 identified in several outcrops, resulting either parallel with or at very low angle to the
325 $S_{2(LHS)}$. Field observations indicate that the abundance of these shear zones, marked
326 by the pervasive occurrence of stretched folds and stretched veins of Qz, significantly
327 increases around Syabrubensi (i.e. approaching the top of the LHS, and within the
328 LHS-Ramgarh Thrust Sheet).
329 Structural features related to the $D_{2(LHS)}$ are overprinted by a $D_{3(LHS)}$ phase
330 represented by a crenulation event and local development of open folds (Fig. 4c).
331 The crenulation lineation $Lcr_{3(LHS)}$ plunges towards NE and E, resting on most of the
332 outcrops at angle <40° with respect to the $L_{2(LHS)}$ (Fig. 4d). The crenulation cleavage
333 $S_{3(LHS)}$ is mostly defined by Bt + Wm. A later $D_{4(LHS)}$ phase is marked by N-S to NW-
334 SE trending folds, usually open, with axes plunging at low/moderate angle to the N
335 and NW and sub-vertical axial planes. In addition, locally aligned Bt, Wm and/or Chl
336 flakes have been observed statically overgrowing the $S_{2(LHS)}$ foliation.
337 Late top-to-the-north extension is recorded by shear band cleavages dipping to the
338 north (Fig. 4e,f) at low angle with respect to the main foliation, and by local
339 development of extension gashes, mainly observed in the Upper-LHS lithologies
340 below the LHS-Ramgarh Thrust Sheet.

4.1.2 Lower Greater Himalayan Sequence

Lithological features

The Lower-GHS lithologies are characterized by highly variable grain size, which is generally coarser than that of the LHS lithologies. The most frequent lithology is a medium-grained two-mica gneissic micaschist with porphyroblastic dark-red Grt ± Ky ± St (Fig. 5a). These rocks exhibit a compositional layering defined by Wm + Bt continuous domains alternating with discontinuous Qz + Pl domains; the main planar foliation is defined by Bt and Wm flakes (up to ~5 mm in length). Locally, a later generation of Wm statically overgrows the planar fabric (Fig. S1a). Ky occurs as large idioblasts, mainly oriented parallel to the main foliation or overgrowing it (Fig. 5**Error! Reference source not found.**b). St is rarely observed at the outcrop scale. Layers of fine-grained two-mica or Bt + Grt -bearing gneisses are often intercalated within these two-mica gneissic micaschists (Fig. 5c); their relative abundance is highly variable, and they range in thickness between few centimetres and several metres.

In the structurally higher levels of the Lower-GHS, fibrolitic Sil appears, especially along the Gosainkund-Helambu transect. The most common lithology at these structural levels is a two-mica + Grt ± Sil micaschist or gneissic micaschist with a well-developed foliation defined by the preferred orientation of Bt, minor Wm ± Sil ± Qz ± Pl concentrated in continuous mm-thick layers, alternated with pluri-mm Qz + Pl ± Kfs ± Bt leucocratic domains (Fig. S1b). Structurally upward in the sequence, microstructures indicating the presence of former melt appear, including leucosomic pods and symplectites related to back-reactions between solids and melt (e.g. Waters, 2001; Cenki *et al*., 2002; Kriegsman and Alvarez-Valero, 2010) and

365 “pseudomorphs after melt” (according to the definition of Holness and Clemens,
366 1999; Holness and Sawyer, 2008) (Fig. 5d).
367 Calc-silicate rocks occur in the Lower-GHS as dm-thick deformed layers or metre-
368 sized massive boudins enveloped by the main schistosity (Fig. 5e). Calc-silicate
369 rocks commonly consist of Grt + Cpx + Pl + Qz (± Zo ± Amph ± Cal), and have a
370 granofelsic structure; a banded structure is observed locally. Layers of quartzites
371 occur in the lowermost part of the Lower-GHS (Fig. 5f). These rocks are especially
372 abundant along the Bothe Khosi River, where they constitute dm- to m- thick layers
373 intercalated in the metapelites. The quartzites are pale-green to greyish and locally
374 banded, with white mica and phlogopite defining the main foliation.
375 In the Gosainkund-Helambu region (Fig. 2), a pluri-km body of a two-mica
376 orthogneiss is hosted within the Lower-GHS metapelites. The orthogneiss shows a
377 well-developed schistosity and cm- to pluri-cm Qz + Fsp eyes, stretched parallel to
378 the main foliation. Where deformation is less pervasive, the porphyric structure of the
379 granitic protolith is still preserved.
380
381 *Structural features*
382 The two-mica + Grt ± Ky ± St gneisses and schists exposed at the lowermost
383 structural levels of the Lower-GHS are intensively deformed and show a pervasive
384 fabric defined by discontinuous Qz + Pl leucocratic domains alternating with dark to
385 grey pluri-mm thick layers consisting of Wm + Bt + Grt ± Ky ± St (Fig. 5a). The
386 compositional banding is often parallel to the main pervasive foliation, here referred
387 to as $S_{2(L\text{-}GHS)}$ and defined by Bt ± Wm ± Ky ± St (Fig. 5a,c). The $S_{2(L\text{-}GHS)}$ derives from
388 the transposition of an earlier foliation $S_{1(L\text{-}GHS)}$. The $S_{1(L\text{-}GHS)}$ is preserved in
389 microlithons, intrafolial folds and isolated fold hinges. The $S_{1(L\text{-}GHS)}$ can be observed

as a compositional banding in quartzites, where it is defined by Wm and Bt, and more rarely in fine-grained gneisses and micaschists. Grt porphyroblasts (up to 2 mm in diameter) are microstructurally in equilibrium with micas defining the $S_{2(L\text{-}GHS)}$. Ky blades, up to several mm in length, have been observed either randomly distributed on the $S_{2(L\text{-}GHS)}$ surface or aligned to define a mineral lineation $L_{2(L\text{-}GHS)}$.

In the orthogneiss, the $S_{2(L\text{-}GHS)}$ is defined by Bt + Wm alignment that envelops deformed K-feldspar and plagioclase porphyroclasts, often defining a pervasive lineation $L_{2(L\text{-}GHS)}$.

On average, the $S_{2(L\text{-}GHS)}$ dips moderately towards NNE and E, dipping steeper in the middle part of the Bothe Khosi valley (Fig. 2). Along the southernmost part of the Helambu transect, the $S_{2(L\text{-}GHS)}$ dips towards S. Biotite, white mica and locally sillimanite define a $L_{2(L\text{-}GHS)}$ down-dip mineral lineation.

The $S_{2(L\text{-}GHS)}$ is deformed by a $D_{3(L\text{-}GHS)}$ folding event, associated with the development of a locally pervasive $S_{3(L\text{-}GHS)}$ crenulation cleavage defined by Bt + Wm (Fig. 6a). The $Lcr_{3(L\text{-}GHS)}$ crenulation lineation and the $F_{3(L\text{-}GHS)}$ fold axes (also identified by S_3-$S_{2(L\text{-}GHS)}$ intersection lineation) plunge moderately to steeply (up to 60°) to the NE and E. In highly deformed areas, the mesoscale $F_{3(L\text{-}GHS)}$ folds are isoclinal to tight, and the $S_{3(L\text{-}GHS)}$ is highly penetrative, transposing the $S_{2(L\text{-}GHS)}$ (Fig. 6b-d). There, localized shear zones are approximately parallel to the $S_{3(L\text{-}GHS)}$, and the $F_{3(L\text{-}GHS)}$ folds show stretched limbs. Aligned biotite and locally kyanite define down-dip mineral lineations on the S_3-$S_{2(L\text{-}GHS)}$ composite foliation. Pinch-and-swell structures of syntectonic quartz veins and foliations related to $D_{2(L\text{-}GHS)}$ and $D_{3(L\text{-}GHS)}$ events are present in several outcrops (Fig. 6). Kinematic indicators (e.g. S-C cleavage relationships, mica-fish, rotated clasts) indicate top-to-the-south sense of shear during both $D_{2(L\text{-}GHS)}$ and $D_{3(L\text{-}GHS)}$ deformation events.

4.1.3 Upper Greater Himalayan Sequence

Lithological features

The most common lithology in the Upper-GHS is Grt + Kfs + Sil migmatitic paragneiss. At the outcrop scale, these rocks typically consist of mm- to cm- thick leucocratic quartz-feldspathic domains alternating with mm- thick dark Bt + Pl + Sil ± Grt layers, which generally define a more or less continuous planar foliation (Fig. 7a). The amount of garnet in the unit is variable. It occurs as mm- to cm-sized porphyroblasts that are often surrounded by a Pl corona (Fig. 7b and Fig. 8i). A late Wm generation locally occurs as large flakes overgrowing the main foliation.

Calc-silicate granofels and gneiss occur as tens of metre thick layers within the hosting metapelites (Fig. 7c). They are easily recognized in the field because of their characteristic deformation styles, due to their relatively weak rheological behaviour compared to the host Qz + Fsp -rich rocks. The main mineral assemblage consists of Cpx + Kfs + Scp ± Pl ± Qz ± Cal, with late green Amph. A banded structure is observed, defined by the different modal proportion of the rock-forming minerals in adjacent layers, possibly reflecting a primary compositional banding.

Large bodies of migmatitic Bt + Sil ± Grt orthogneiss, that are concordant with the regional foliation, are present at different structural levels. Metre- to tens of metre thick layers of fine-grained biotitic gneiss with Sil-rich nodules (“Black Gneisses” according to Lombardo et al., 1993) are sometimes associated with the orthogneiss (Fig. 7d). The nodules, up to several cm in length, mainly consist of Sil + Qz and are flattened parallel to the foliation. Pegmatitic dykes and two-mica + Grt + Tur leucogranite bodies and dykes occur at the higher structural levels of the Upper-GHS, and are variably oriented with respect to the main foliation. These

leucogranites are the dominant lithology in the highest peaks of the Langtang Valley (e.g. Langtang Lirung, Langtang II, Kimshung).

Structural features

The various penetrative structures occurring in the high-grade, often migmatitic, Upper-GHS lithologies are difficult to be univocally interpreted at the mesoscale due to the interplay between melt-producing processes, melt-crystallizing processes and tectonic processes. Relicts of a foliation older than the main pervasive foliation have not been observed, perhaps reflecting complete transposition. It is therefore not possible to ascribe the main regional schistosity to a specific deformational phase, and to correlate it with the planar fabrics observed in the LHS and in the Lower-GHS units. In other words, it is not possible to understand if the main foliation is a $S_{1(U\text{-}GHS)}$ or a $S_{2(U\text{-}GHS)}$, therefore the neutral term $S_{m(U\text{-}GHS)}$ (main schistosity) has been preferred.

The migmatites are characterized by a banded structure, defined by Bt + Sil + Qz ± Grt mm-thick mesocratic domains, alternating with Qz + Pl + Kfs ± Sil ± Grt pluri-mm leucocratic layers (Fig. 7a,e,f). The $S_{m(U\text{-}GHS)}$ planar fabric is parallel to the compositional layering and is marked by the alignment of Bt and fibrolitic Sil. Leucosomes are almost parallel to the $S_{m(U\text{-}GHS)}$ and contain a planar fabric defined by biotite, thus suggesting that melting was contemporary to the $S_{m(U\text{-}GHS)}$ development.

Calc-silicate rocks are either stretched and deformed (Fig. 7c), or, more rarely, form boudins enveloped by the $S_{m(U\text{-}GHS)}$, depending on their mineral assemblage. The migmatitic orthogneisses often show a mylonitic fabric, with clasts of Kfs stretched and rotated. In these rocks, S-C structures suggest top-the S/SW sense of shear. A

mineral lineation $L_{m(U\text{-}GHS)}$ is locally defined by Bt, Sil, Sil-rich nodules (Fig. 6d) and/or Fsp, plunging parallel to the $S_{m(U\text{-}GHS)}$ dip. The dominant $S_{m(U\text{-}GHS)}$ is deformed by open to tight folds, with fold axes often striking NE-SW and axial planes plunging moderately to the north. In several ouctrops, the $S_{m(U\text{-}GHS)}$ is cross-cut by discrete top-to-the-south shear band cleavages, with white mica growing along the C-planes (Fig. 7f).

4.2 Petrography and mineral chemistry

Microstructural features of samples 15-19, 15-28b, 15-26b, 15-38 and 14-12 are briefly discussed in this section, whereas those of the other samples (14-27a,14-03, 14-25b, 14-24, 14-44a, 14-61b, 14-71, 14-52, 14-08a) are presented by Rapa et al. (2016) and are summarized in Table 1. Mineral chemistry for all the samples is summarized in Table 2. Garnet chemical profiles of all the samples are given in Fig. S2a-d.

4.2.1 Sample 15-19: Bt + Wm + Grt micaschist (LHS)

Sample 15-19 is a fine-grained micaschist, consisting of Bt, Wm, Grt, Qz, Pl, Chl and accessory Ilm and Tur. The well-developed foliation ($S_{2(LHS)}$) is defined by the preferred orientation of Bt and Wm, concentrated in continuous sub-mm-thick layers, alternating with discontinuous mm-thick layers rich in Qz and Pl (Fig. 8a). Locally, Qz aggregates, few-mm in thickness and with a granoblastic structure, could represent boudinated and transposed, pre-$S_{2(LHS)}$ Qz veins. Grt porphyroblasts (up to 2 mm in diameter) are dispersed in the matrix; they have a skeletal habit and are partly wrapped by the main foliation. Grt includes an internal rotated foliation ($S_{1(LHS)}$: snow-ball microstructure) defined by the alignment of Qz, Pl and Ilm. Pl is abundant and

often shows a granoblastic habit (Fig. S1c); larger porphyroblasts locally overgrow the main foliation. Large Chl and Wm flakes statically overgrow $S_{2(LHS)}$ (Fig. S1d); Chl also replaces Bt and Grt rims (Fig. 8a).

4.2.2 Sample 15-28b: Bt + Wm + Grt + Ky + St micaschist (LHS)

Sample 15-28b is a fine-grained two-mica phyllitic micaschist, consisting of Qz, Grt, Wm, Bt, Ky, St and accessory Gr, Tur and Ilm. The main schistosity ($S_{2(LHS)}$) is defined by the preferred orientation of Wm and Bt in continuous sub-mm-thick layers alternating with discontinuous mm-thick Qz domains (Fig. 8b). $S_{2(LHS)}$ transposes an older foliation ($S_{1(LHS)}$) preserved in few microlithons and defined by both Wm and Bt (Fig. 8c). The main foliation is further crenulated and overprinted by a later, pluri-mm spaced planar foliation ($S_{3(LHS)}$). $S_{3(LHS)}$ is defined by Wm and Bt (Fig. S1e) and developed at high angle with respect to $S_{2(LHS)}$. Grt porphyroblasts are centimetric in size (up to 1 cm in diameter, Fig. 8b); they are idioblastic in the micaceous layers, while they have a skeletal habit in the Al-poor, quartzitic domains. Grt includes an internal foliation defined by Qz, Ilm, Gr and Wm, which is continuous with the external $S_{2(LHS)}$; it also includes St and minor Ky at its rims (Fig. 8c). St and Ky occur both as inclusions in the Grt rims and in the matrix; St includes Qz, Wm, Ilm and Gr. Ky in the matrix may include Qz and Ilm.

4.2.3 Sample 15-26b: Bt + Wm + Grt gneissic micaschist (LHS-Ramgarh Thrust Sheet)

Sample 15-26b is a medium-grained micaschist, consisting of Qz, Pl, Bt, Grt, minor Wm, accessory Rt and Ilm and minor late Chl and Sil. The main foliation ($S_{2(LHS)}$) is defined by the preferred orientation of Bt and Wm concentrated in continuous, mm-

thick layers, alternating with few-mm-thick discontinuous Qz + Pl domains (Fig. 8d). Grt porphyroblasts (up to 2 mm in diameter) are abundant and dispersed in the matrix. They are partially wrapped by the main foliation and include Qz, Rt, Ilm and minor Bt, Wm and Pl (Fig. 8e). Grt rims are typically in equilibrium contacts with the matrix. Pl is in equilibrium with the $S_{2(LHS)}$; it rarely includes Qz, Bt, Wm and Rt. An acicular aluminosilicate, possibly Sil, locally grows at the Pl–Wm interfaces; in the same microstructural position, symplectites consisting of Qz + Kfs rarely occur. Rt and Ilm are present both as inclusions in Grt and in the matrix and Ilm often replaces Rt in the matrix; rare Chl replaces Bt and Grt rims.

4.2.4 Sample 15-38: Wm + Bt + Ky + St micaschist, with poprhyroblastic Grt (Lower-GHS)

Sample 15-38 is a coarse-grained micaschist consisting of Wm, Qz, Grt, Bt, Pl and minor Ky and St, with accessory Rt, Ilm and Turm. The main foliation ($S_{2(L\text{-}GHS)}$) is defined by the preferred orientation of Wm and Bt flakes concentrated in pluri-mm continuous layers, alternating with mm-thick Qz and Pl domains.

Grt occurs both as large porphyroblasts (up to 4 mm in diameter) partially wrapped by the main foliation (Fig. 8f), and as small idioblasts (up to 1 mm in diameter) that show equilibrium relationships with Wm and Bt (Fig. S1f). Grt porphyroblasts are crowded with inclusions (Grt cores: Qz, Pl, Wm and minor Bt, Rt and Ilm; Grt rims: Qz, Wm, Pl, minor Bt and St, Rt and Ilm; Fig. S1h).

Locally, a later generation of Wm occurs as large flakes (up to 2 mm) overgrowing $S_{2(L\text{-}GHS)}$. Ky is scarce, but where present it occurs as large bladed flakes (up to 3 mm in length) oriented generally parallel to the main foliation. Ky is always replaced by Wm (Fig. 8g) and/or Pl at its rims and it locally includes Bt. St is also scarce; it occurs

both as inclusions in Grt rims (Fig. S1h) and in the matrix as crystals up to 2 mm in length and including Pl, Qz and Rt (Fig. 8g). Pl is abundant, occurs as subhedral crystals and it locally includes Qz (Fig. S1g). Rare Sil replaces Grt rims (Fig. S1h). Accessory Rt and minor Ilm occur both as inclusions in Grt and in the matrix. Rt is often replaced by Ilm (Fig. S1h).

4.2.5 Sample 14-12: Bt + Grt + Sil migmatite (Upper-GHS)

Sample 14-12 is a medium-grained Bt + Sil + Grt + Pl + Kfs + Qz migmatitic gneiss, with late Wm and accessory Ilm. It is characterized by a banded structure (Fig. 8h) defined by Bt + Sil + Qz ± Grt mm-thick mesocratic domains, alternating with Qz + Pl+ Kfs ± Sil ± Bt pluri-mm leucocratic domains. The main foliation ($S_{m(U\text{-}GHS)}$) is parallel to the compositional layering and is defined by the preferred orientation of Bt lepidoblasts and fibrolitic Sil. Grt porphyroblasts (up to 2 mm in diameter) are skeletal and contain large polymineralic inclusions of Qz + Bt + Pl (Fig. 8i). Bt in the matrix is locally overgrown by large flakes of Wm. Pl and Kfs are mainly concentrated in the leucocratic domains though Pl is also observed replacing Grt rims (Fig. 8i). Myrmekitic structures occur at the interface between Kfs and Pl (Fig. S1i).

The mesocratic domains are characterized by the occurrence of Bt + Qz + Sil + Pl symplectites developed at the expenses of Kfs and of Wm + Qz + Pl symplectites developed at the expenses of Kfs and Grt (Fig. S1l).

4.3. P-T evolution of LHS, LHS-Ramgarh Thrust Sheet, Lower-GHS and Upper-GHS units

The P-T evolution of the studied samples was constrained using two independent methods: optimal thermobarometry (i.e. AvPT) and the pseudosection approach. Our

565 aim was to test if tectonometamorphic discontinuities might be detected using the
566 relatively fast AvPT approach, which allows application of relative thermobarometry
567 on a large number of samples, as an alternative to the more laborious and time
568 consuming pseudosection approach.
569
570 ***4.3.1 Optimal thermobarometry***
571 ***LHS*** - In the LHS phyllitic micaschists (samples 15-19, 14-27a and 15-28b), both the
572 prograde and the peak equilibrium assemblages (defining the $S_{1(LHS)}$ and the $S_{2(LHS)}$
573 foliations, respectively) define enough equilibria to converge to an AvPT result (§3.3).
574 The obtained *P-T* results are similar for all the samples: the prograde $S_{1(LHS)}$
575 development is estimated at about 540°C and 6.6-7.0 kbar, while peak P-T
576 conditions occurred at about 590-600°C and 7.1-8.2 kbar (Fig. 9a,b, Fig. 10a,b and
577 Table 3). Overall, the LHS samples recorded a prograde P-T evolution characterized
578 by an increase in both P and T up to the peak of metamorphism, corresponding to a
579 T/P ratio of 80 °C/kbar (Table 4b).
580 ***LHS-Ramgarh Thrust Sheet*** - Sample 15-26b, exposed within the Ramgarh Thrust
581 Sheet just below the MCT, gives higher P-T conditions for both the prograde and
582 peak assemblages, with respect to the other LHS samples. Specifically, prograde P-
583 T conditions are estimated at about 585°C, 7.8 kbar, while peak P-T conditions
584 occurred at 600°C, 8.8 kbar (Fig. 9a,b, Fig. 10a,b and Table 3). The geometry of the
585 prograde P-T path is nevertheless similar to that of the other LHS samples, but the
586 T/P ratio is lower (69 °C/kbar, Table 4b).
587 ***Lower-GHS*** - The Lower-GHS metapelitic samples (14-03, 14-25b, 14-24, 15-38, 14-
588 44a, 14-61b, 14-71) recorded peak *P-T* conditions in the range 660-710°C, 8.3-9.8
589 kbar, with a slight increase in both P and T proceeding structurally upward in the

590 transect (Fig. 9c-f, Fig. 10a,b and Table 3). The structurally lowermost samples (14-
591 03, 14-25b and 15-38) preserve evidence of their prograde history at 585-640°C, 6.4-
592 7.8 kbar (Fig. 9c-d, Table 3).The structurally higher samples do not preserve
593 evidence of their prograde evolution. Lowering the aH_2O to 0.9 to simulate the
594 occurrence of incipient partial melting at peak conditions, would result in a decrease
595 of both T and P of about 10-15°C, 0.1-0.5 kbar (Table 3). The estimated peak
596 metamorphic conditions correspond to a T/P ratio of about 76 °C/kbar (Table 4b).
597 The structurally uppermost sample 14-52 records unusually high peak P-T conditions
598 (850 ± 68°C, 11.3 ± 2.7 kbar), but also shows the highest uncertainties. These P-T
599 conditions are unrealistic because this sample does not show evidence of partial
600 melting (Rapa et al., 2016). It is likely that AvPT failed in calculating peak P-T
601 conditions for this sample because it does not contain Wm, probably deriving from a
602 Bt-rich protolith.
603 ***Upper-GHS*** - The Upper-GHS samples (14-08a and 14-12) do not preserve relics of
604 their prograde history, and experienced various degrees of partial melting. These
605 samples recorded peak P-T conditions of 800-815°C, ~6 kbar (Fig. 9c,d, Fig. 10a,b
606 and Table 3), well within the Sil-stability field, defining a T/P ratio of 134 °C/kbar (Fig.
607 9c,d, Table 3and Table 4b).
608 The uncertainties (2σ values) associated to the AvPT results are generally greater
609 than ± 20°C and ± 1 kbar; these relatively large uncertainties might be due to several
610 factors, including analytical uncertainties or uncertainties in the thermodynamic data
611 and in the activity-composition relationships (e.g. Fraser et al., 2000). However, it is
612 worth noting that *P-T* conditions independently constrained using the pseudosection
613 approach (see Rapa et al., 2016 and the following Section 4.3.2) plot very close to, or
614 totally within the uncertainties of, the AvPT results (Fig. 10a,b).

615

616 ***4.3.2 P-T pseudosections***

617 P-T pseudosections have been modeled by Rapa et al. (2016) for nine of the 14
618 samples investigated in this study. Additional P-T pseudosections have been
619 calculated in this study for sample 15-26b, because Rapa et al. (2016) didn't
620 investigate the P-T evolution of the LHS-Ramgarh Thrust Sheet. The bulk-rock
621 composition of sample 15-26b was calculated by combining mineral modes and
622 compositions (see Rapa et al., 2016 for methodology). Two pseudosections have
623 been calculated for this sample to account for the fractionation effects on the bulk
624 composition due to the growth of zoned garnet porphyroblasts. The pseudosection
625 calculated for the unfractionated bulk composition (Fig. 11a,b) gives information
626 about the mineral assemblage stable during the prograde growth of Grt core, which
627 includes Bt, Wm, Pl, Rt ± Ilm. This assemblage is stable in the Bt ± Chl + Pl + Ms ±
628 Pg + Grt + Qz + Rt + H_2O fields, at T>450°C. Grt core compositional isopleths
629 (XMg=0.09-0.11, XCa=0.17-0.20, XMn=0.09-0.07; Fig. S2a) further constrain the *P-T*
630 conditions of the prograde Grt growth at T=550-575°C and P=7.5-8.5 kbar, in the Bt +
631 Chl + Pl + Ms + Grt + Qz + Rt field. Chl has not been observed included in Grt in this
632 sample because it was completely consumed during prograde metamorphism.
633 Growth of Grt rim in the quini-variant Bt + Pl + Ms + Grt + Qtz + Rt field (Fig. 11c) is
634 consistent with the interpreted equilibrium between Grt rim and Bt, Ms, Pl and Rt (±
635 Ilm). Compositional isopleths (XMg=0.13–0.14; XCa=0.16–0.14; XMn=0.03–0.04;
636 Fig. S2b) constrain the growth of Grt rim at peak *P-T* conditions of 620–650°C, 8.7–
637 10.4 kbar (Fig. 11c, Table 4a). Both Grt core and Grt rim are predicted to grow at
638 sub-solidus conditions (Fig. 11d), in agreement with microstructural observations.

639

5. DISCUSSION

5.1 Comparison between AvPT and pseudosection results

The comparison between peak P-T conditions constrained using the AvPT method and those constrained using the pseudosection approach is reported in Table 4 and Fig. 10a,b. The two methods give consistent results relative to one another, although the absolute P-T values are slightly different; peak P-T conditions estimated with the AvPT method are generally lower than those estimated using the pseudosection approach (Fig. 10a,b). Peak temperatures constrained with both methods gradually increase structurally upward, passing from 590-600°C in the LHS to 610-640°C in the LHS-Ramgarh Thrust Sheet, 700-740°C in the Lower-GHS and 780-810°C in the Upper-GHS. In addition, both methods highlight pressure breaks in both the LHS and GHS sequences. Specifically, peak pressures in the LHS-Ramgarh Thrust Sheet (8.8-9.6 kbar) are higher than those registered in the lowermost LHS (7.4-7.5 kbar), whereas peak pressures in the Upper-GHS (6.1-7.8 kbar) are lower than those registered in the lowermost Lower-GHS (9.3-10 kbar). This implies significantly different T/P ratios for the four units (see the following section 5.2). The T/P ratios obtained with the AvPT method are remarkably similar to those obtained using the pseudosection approach as concerning the LHS, LHS-Ramgarh Thrust Sheet and Lower-GHS samples (Table 4); the AvPT results for Upper-GHS samples define a higher T/P ratio with respect to that constrained using pseudosections (134 ± 41 °C/kbar *vs.* 101 ± 12 °C/kbar), due to the large uncertainties in the AvPT estimates. Both methods are therefore useful to recognise rock packages characterized by different peak P-T conditions, although uncertainties related to the AvPT results are larger than those related to the pseudosection results (i.e. absolute P-T values obtained using pseudosections are more reliable than those obtained using AvPT).

665 The AvPT method is faster to apply than the pseudosection approach, thus allowing
666 to focalize the following more precise – but also more time consuming, more
667 expensive and more complex – studies (e.g. pseudosections, geochronology, etc.)
668 on specific and selected areas only. Conversely, the main advantage of the
669 pseudosection approach over the AvPT method is the possibility of reconstructing the
670 whole P-T evolution of the studied samples (i.e. prograde and/or retrograde *P–T*
671 evolution), which can outline the differences and similarities of *P–T* paths in a set of
672 samples otherwise only grouped by coherent peak *P–T* conditions.
673
674 **5.2 Petrological and structural criteria for identifying tectonometamorphic**
675 **discontinuities within the LHS and the GHS**
676 Peak *P–T* conditions obtained for the studied samples using the pseudosection
677 approach and the AvPT method highlight the existence of four different T/P ratio
678 populations of 80 ± 11 °C/kbar (LHS), 66 ± 7 °C/kbar (LHS-Ramgarh Thrust Sheet),
679 73 ± 1 °C/kbar (Lower-GHS) and 101 ± 12 °C/kbar (Upper-GHS), respectively (Fig.
680 10c and Table 4). These values are partially overlapped within errors (Fig. 10c),
681 because of the relatively large errors associated to the weighted average values
682 estimated for each population. However, these errors would be reduced, and the
683 difference between populations would be consequently enhanced, if more samples
684 are considered for each unit (e.g. compare the small error associated to the Lower-
685 GHS, for which eight samples have been considered, with the relatively large error
686 associated to the LHS-Ramgarh Thrust Sheet, for which only one sample was
687 considered). Furthermore, even considering the partially overlapped T/P ratio values,
688 the different populations can be easily recognized by combining the T/P ratios with
689 the absolute T estimates (i.e. T < 650°C for the LHS and LHS-Ramgarh Thrust

690 Sheet; T > 650°C for the Lower-GHS). Finally, it is worth noting that our results are in
691 good agreement with those calculated using the P-T results of Kohn (2008) for
692 samples collected from the same structural levels in the Langtang region (ZL1-3: 71 ±
693 6 °C/kbar; ZL4: 55 ± 3 °C/kbar; ZG1 and ZG2: 63 ± 3 °C/kbar; ZG3 and ZG4: 92 ± 8
694 °C/kbar; P-T data obtained using the conventional thermobarometry approach; see
695 also Fig. 10), thus confirming the statistical difference between T, P and T/P ratios
696 estimated for each unit. Rock packages recording different T/P ratios are also
697 characterized by different P-T evolutions (see also Rapa et al., 2016) (Fig. 12). The
698 P-T paths recorded by LHS and LHS-Ramgarh Thrust Sheet samples have a similar
699 hairpin shape, although that of the LHS-Ramgarh Thrust Sheet unit is shifted towards
700 higher P-T conditions. The Lower-GHS samples describe a clockwise P-T trajectory
701 mostly in the Ky stability field. Their prograde evolution, characterized by an increase
702 in both T and P, is only recorded by the structurally lower samples, whereas the
703 retrograde evolution is well preserved in all the samples. The Upper-GHS samples
704 recorded a clockwise P-T path, but in the Sil stability field, characterized by nearly
705 isobaric heating associated with partial melting processes (Rapa et al., 2016).
706 Overall, petrological data are consistent with the existence of three metamorphic
707 discontinuities which separate the LHS from the LHS-Ramgarh Thrust Sheet (lower
708 discontinuity), the LHS-Ramgarh Thrust Sheet from the Lower-GHS (intermediate
709 discontinuity) and the Lower-GHS from the Upper-GHS (upper discontinuity).
710 Mesostructural data show that the lower and intermediate metamorphic
711 discontinuities also coincide with pervasive syn-metamorphic deformation (e.g.
712 mylonitic foliation, mesoscopic shear zones, occurrence of different stretched
713 lithological bodies) with a consistent top-to-the-south sense of shear, thus indicating
714 that these metamorphic discontinuities also coincide with structural discontinuities.

715 Mesostructural data for the upper discontinuity are more ambiguous, because of the
716 interplay between tectonic, melt-producing and melt-crystallizing processes which
717 occurred in the high-grade, often migmatitic, Upper-GHS lithologies. However, a
718 consistent top-to-the-south sense of shear is recorded by widespread asymmetric
719 boudinage, asymmetry of folds and S-C structures.
720 The lower discontinuity outlined in the study area can be identified with the Ramgarh
721 Thrust (Munsiari Thrust in Kohn, 2008), which separates a package of LHS rocks in
722 its hanging wall (LHS-Ramgarh Thrust Sheet) that experienced peak metamorphism
723 at higher P-T conditions (~635°C, 10 kbar) than the other LHS rocks in its foot wall
724 that experienced peak metamorphism at lower P-T conditions (~600°C, 7.5 kbar).
725 The intermediate discontinuity coincides with the MCT, which separates the LHS
726 from the GHS. The MCT is marked by an abrupt increase in both peak P and T, up to
727 740°C, 9.5-10.5 kbar over a structural distance of less than 2 km. The upper
728 discontinuity is defined as Langtang Thrust (Kohn et al., 2005) and separates the
729 Lower-GHS from the Upper-GHS, which experienced significantly different peak
730 metamorphic conditions and P-T evolutions (Lower-GHS: 700-740°C, 9.5-10.5 kbar,
731 prograde increase in both P and T in the kyanite stability field; Upper-GHS: 780-
732 800°C, 7.5-8.0 kbar; nearly isobaric heating in the sillimanite stability field).
733
734 **5.3 Thrusting kinematics of the study area**
735 In the study area, the Ramgarh Thrust and MCT are sub-parallel, with a NW-SE trend
736 north of Syabrubensi, becoming roughly N-S towards the south. Conversely, the
737 strike of the Langtang Thrust changes from NW-SE to roughly E-W (Fig. 2). The
738 spatial disposition of these three main structural and metamorphic discontinuities
739 characterizes the tectonic architecture of the area. The north-dipping Lower-GHS is

few km thick in the Gatlang-Langtang region. It dips flattens progressively towards the Gosainkund-Helambu region where it is more broadly exposed (see also Rapa et al., 2016) and then it becomes south-dipping on the northern side of the synformal Kathmandu Nappe, in the Kathmandu area (Fig. 1 and Fig. 2). Geological and petrological constraints (Rapa et al., 2016 and references therein) support a Kathmandu Nappe configuration in which the Lower-GHS rocks are directly overlaid by a succession (Bhimpedi-Phulchauki group) interpreted as correlative to the TSS. The juxtaposition of this portion of TSS on the Lower-GHS occurs across a shear zone (Galchi shear zone of Webb et al., 2011), which corresponds to the southern prolongation of the STDS. It merges with the MCT along the northern margin of the Kathmandu Nappe (e.g. Johnson et al., 2001; Webb et al., 2011; He et al., 2015). As for other sectors of the Himalaya , this tectonometamorphic architecture is result from the development of multiple south-verging thrusts, including intra-GHS thrusting, juxtaposition of the GHS onto the LHS and the formation of foreland-directed LHS duplex structures at the regional scale (e.g. Schelling and Arita, 1991; Pearson and DeCelles, 2005; Khanal et al., 2015).

Detailed geochronological data (monazite U-Pb ages) presented by Kohn et al. (2004, 2005) and Kohn (2004, 2008) for the Gatlang-Langtang transect show that the age of peak metamorphism is progressively younger towards lower structural levels (Upper-GHS: 25-21 Ma; Lower-GHS: 24-17 Ma; LHS-Ramgarh Thrust Sheet: 13-10 Ma; LHS: 4-3 Ma). Moreover, titanite U-Pb ages obtained from a Lower-GHS calc-silicate rock exposed in the adjacent Gosainkund-Helambu region consistently point to peak metamorphic ages of 19-20 Ma (Rapa et al., 2017). These ages support an in-sequence thrusting interpretation for all the tectonometamorphic discontinuities recognized in the area. The movement along the Ramgarh Thrust is constrained to

765 have occurred after the intra-GHS thrusting and the MCT activation (Kohn et al.,
766 2004). The formation of the LHS duplexing can be constrained between 10-3 Ma and
767 ended with the activation of the MBT to the south (<3 Ma). The $D_{3(LHS)}$ folding event
768 (roughly characterized by NE-SW striking axis) interpreted in this study, can be
769 tentatively correlated with duplex formation. The present steep dips of the Ramgarh
770 Thrust and MCT in the Langtang region may reflect a late tilting on the northern
771 ramps during the in-depth emplacement of LHS thrust sheets and the growing of a
772 large-scale antiform because of $D_{3(LHS)}$ and $D_{4(LHS)}$ interferences (Fig. 1).
773 In this setting, the extensional features identified in the upper LHS and in the LHT-
774 Ramgarh Thrust Sheet, developed mainly in a brittle-ductile regime, define an
775 extensional regime parallel to the orogen during an overall shortening.
776

777 **6. Conclusions**

778 Overall, data and results presented in this paper demonstrate that petrological and
779 structural analysis are capable of identifying tectonometamorphic discontinuities in
780 the LHS and GHS, thus allowing their fast detection. Such discontinuities are marked
781 by: (i) contrasting T/P ratios, peak P-T conditions and P-T paths in the footwall and
782 hanging-wall; (ii) an increase in the intensity of deformation, with development of
783 pervasive mylonitic fabrics and/or shear zones, in proximity to the discontinuity.
784 Geochronological data are not necessarily required to identify such discontinuities,
785 but become indispensable for the interpretation of their nature (e.g. in-sequence vs.
786 out-of-sequence thrust) and for the reconstruction of kinematic models.
787

788 **ACKNOWLEDGEMENTS**

789 Fieldwork and laboratory work was supported by the University of Torino (Ricerca
790 Locale, ex-60% -2014, 2015 funds: ROLF_RILO_15_01, GROC_RILO_16_01) and

Compagnia di San Paolo (University of Torino, Call 1, Junior PI Grant: TO_Call1_2012_0068), by the Italian Ministry of University and Research (PRIN 2011: 2010PMKZX7) and by Ev-K2-CNR (SHARE Project) in collaboration with the Nepal Academy of Science and Technology. K. Larson and an anonymous reviewer are kindly acknowledged for their constructive comments which improved the manuscript.

REFERENCES

Ambrose, T.K., Larson, K.P., Guilmette, C., Cottle, J.M., Buckingham, H., Rai, S., 2015. Lateral extrusion, underplating, and out-of-sequence thrusting within the Himalayan metamorphic core, Kanchenjunga, Nepal. Lithosphere 7, 441-464.

Auzanneau, E., Schmidt, M.W., Vielzeuf, D., Connolly, J.A.D., 2010. Titanium in phengite: a geobarometer for high temperature eclogites. Contributions to Mineralogy and Petrology 159, 1–24.

Carosi, R., Montomoli, C., Visonà, D., 2007. A structural transect in the Lower Dolpo: insights on the tectonic evolution of Western Nepal. Journal of Asian Earth Science 29, 407–423.

Carosi, R., Montomoli, C., Rubatto, D., Visonà, D., 2010. Late oligocene high-temperature shear zones in the core of the Higher Himalayan Crystallines (Lower Dolpo, western Nepal). Tectonics 29, TC4029.

Catlos, E.J., Harrison, T. M., Kohn, M.J., Grove, M., Ryerson, F.J., Manning, C.E., Upreti, B. N., 2001. Geochronologic and thermobarometric constraints on the evolution of the Main Central Thrust, central Nepal Himalaya. Journal of Geophysical Research: Solid Earth 106, 16177– 16204.

Catlos, E.J., Harrison, T. M., Manning, C.E., Grove, M., Rai, S.M., Hubbard, S.M., Upreti, B.N., 2002. Records of the evolution of the Himalayan orogen from in situ Th–Pb ion microprobe dating of monazite: Eastern Nepal and western Garhwal. Journal of Asian Earth Science 20, 459-479.

Cenki, B., Kriegsman, L.M., Braun, I., 2002. Melt-producing and melt-consuming reactions in the Achankovil cordierite gneisses, South India. Journal of Metamorphic Geology 20, 543–561.

823 Coggon, R., Holland, T.J.B., 2002. Mixing properties of phengitic micas and revised
824 garnet–phengite thermobarometers. Journal of Metamorphic Geology 20, 683–
825 696.
826 Connolly, J.A.D., 1990. Multivariable phase diagrams: an algorithm based on
827 generalized thermodynamics. American Journal of Science 290, 666–718.
828 Connolly, J.A.D., 2009. The geodynamic equation of state: what and how.
829 Geochemistry Geophysics Geosystems 10, Q10014.
830 Daniel, C.G., Hollister, L., Parrish, R.R. , Grujic, D., 2003. Exhumation of the Main
831 Central thrust from lower crustal depths, Eastern Bhutan Himalaya. Journal of
832 Metamorphic Geology 21, 317–334.
833 Davidson, C., Grujic, D., Hollister, L., Schmid, S.M., 1997. Metamorphic reaction
834 related to decompression and synkinematic intrusion of leucogranite, high
835 Himalayan Cristallines, Bhutan. Journal of Metamorphic Geology 15, 593–612.
836 DeCelles, P.G., Robinson, D.M., Quade, J., Ojha, T.P., Garzione, C.N., Copeland, P.,
837 Upreti, B.N., 2001. Stratigraphy, structure and tectonic evolution of the Himalayan
838 fold–thrust belt in western Nepal. Tectonics 20, 487–509.
839 Fraser, G., Worley, B., Sandiford, M., 2000. High-precision geothermobarometry
840 across the High Himalayan metamorphic sequence, Langtang Valley, Nepal.
841 Journal of Metamorphic Geology 18, 665–681.
842 Gaetani, M., Garzanti, E., 1991. Multicyclic history of the northern India continental
843 margin (north- western Himalaya). AAPG Bulletin 75, 1427–1446.
844 Gansser, A., 1983, Geology of the Bhutan Himalaya: Birkhäuser Verlag, Basel, 181
845 pp.
846 Godin, L., Grujic, D., Law, R.D., Searle, M. P., 2006. Channel flow, ductile extrusion
847 and exhumation in continental collision zones: an introduction. In: Law, R.D.,

Searle, M.P., Godin, L. (Eds.) Channel flow, ductile extrusion and exhumation in continental collision zones. Geological Society of London Special Publications 268, pp. 1–23.

Goscombe, B., Hand, M., 2000. Contrasting P-T paths in the Eastern Himalaya, Nepal: inverted isograds in a paired metamorphic mountain belt. Journal of Petrology 41, 1673–1719.

Goscombe, B., Gray, D., Hand, M., 2006. Crustal architecture of the Himalayan metamorphic front in eastern Nepal. Gondwana Research 10, 232–255.

Groppo, C., Rolfo, F., Lombardo, B., 2009. P-T evolution across the Main Central Thrust Zone (Eastern Nepal): hidden discontinuities revealed by petrology. Journal of Petrology 50, 1149–1180.

Groppo, C., Rubatto, D., Rolfo, F., Lombardo, B. , 2010. Early Oligocene partial melting in the Main Central Thrust Zone (Arun Valley, eastern Nepal Himalaya). Lithos 118, 287-301.

Groppo, C., Rolfo, F., Indares, A., 2012. Partial melting in the Higher Himalayan Crystallines of Eastern Nepal: the effect of decompression and implications for the ‘‘channel flow’’ model. Journal of Petrology 53, 1057–1088.

Groppo, C., Rolfo, F., Mosca, P., 2013. The cordierite-bearing anatectic rocks of the Higher Himalayan Crystallines (eastern Nepal): low-pressure anatexis, melt-productivity, melt loss and the preservation of cordierite. Journal of metamorphic Geology 31, 187–204.

Guillot, S., 1999. An overview of the metamorphic evolution of Central Nepal. Journal of Asian Earth Sciences 17, 713-725.

871 Harrison, T.M., Ryerson, F.J., Le Fort, P., Yin, A., Lovera, O.M., Catlos, E.J., 1997. A
872 late Miocene–Pliocene origin for the Central Himalayan inverted metamorphism.
873 Earth and Planetary Science Letters 146, E1–E7.
874 He, D., Webb, A.A.G., Larson, K.P., Martin, A.J., Schmitt, A.K., 2015. Extrusion vs.
875 duplexing models of Himalayan mountain building. 3: Duplexing dominates from
876 the Oligocene to Present. International Geology Review 57, 1–27.
877 Hodges, K., 2000. Tectonics of Himalaya and southern Tibet from two perspectives.
878 Geological Society of American Bullettin 112, 324–350.
879 Holland, T.J.B., Powell, R., 1998. An internally consistent thermodynamic data set for
880 phases of petrologic interest. Journal of Metamorphic Geology 16, 309–343.
881 Holland, T.J.B., Powell, R., 2001. Calculation of phase relations involving
882 haplogranitic melts using an internally consistent thermodynamic dataset. Journal
883 of Petrology 42, 673–683.
884 Holland, T.J.B., Powell, R., 2011. An improved and extended internally consistent
885 thermodynamic dataset for phases of petrological interest, involving a new equation
886 of state for solids. Journal of Metamorphic Geology 29, 333– 383.
887 Holland, T., Baker, J., Powell, R., 1998. Mixing properties and activity-composition
888 relationships of chlorites in the system MgO-FeO-Al2O3-SiO2-H2O. European
889 Journal of Mineralogy 10, 395–406.
890 Holness, M.B., Clemens, J.D., 1999. Partial melting of the Appin Quartzite driven by
891 fracture controlled H_2O infiltration in the aureole of the Ballachulish Igneous
892 Complex, Scottish Highlands. Contributions to Mineralogy and Petrology 136,
893 154–168.
894 Holness, M.B., Sawyer, E.W., 2008. On the pseudomorphing of melt-filled pores
895 during the crystallization of migmatites. Journal of Petrology 49, 1343–1363.

Iaccarino, S., Montomoli, C., Carosi, R., Massonne, H-J., Visonà, D., 2017. Geology and tectonometamorphic evolution of the Himalayan metamorphic core: insights from the Mugu Karnali transect, Western Nepal (Central Himalaya). Journal of Metamorphic Geology 35, 301-325.

Imayama, T., Takeshita, T., Arita, K., 2010. Metamorphic P–T profile and P–T path discontinuity across the far-eastern Nepal Himalaya: investigation of channel flow models. Journal of Metamorphic Geology 28, 527–549.

Imayama, T., Takeshita, T., Yi, K., Cho, D.-L., Kitajima, K., Tsutsumi, Y., Kayama, M., Nishido, H., Okumura, T., Yagi, K., Itaya, T., Sano, Y., 2012. Two-stage partial melting and contrasting cooling history within the Higher Himalayan Crystalline Sequence in the far-eastern Nepal Himalaya. Lithos 134-135, 1–22.

Inger, S., Harris, N.B.W., 1992. Tectonothermal evolution of the High Himalayan Crystalline Sequence, Langtang Valley, northern Nepal. Journal of Metamorphic Geology 10, 439–452.

Jessup, M.J., Law, R.D., Searle, M.P., Hubbard, M.S., 2006. Structural evolution and vorticity of flow during extrusion and exhumation of the Greater Himalayan Slab, Mount Everest Massif, Tibet/Nepal: implications for orogen-scale flow partitioning. In: Law, R.D., Searle, M.P., Godin, L. (Eds.), Channel Flow, Extrusion, and Exhumation in Continental Collision Zones. Geological Society of London Special Publications 268, pp. 379-414.

Johnson, M. R. W., Oliver, G. J. H., Parrish, R. R., Johnson, S. P., 2001. Synthrusting metamorphism, cooling, and erosion of the Himalayan Kathmandu Complex, Nepal. Tectonics 20, 394–415.

Khanal, S., Robinson, D.M., Kohn, M.J., Mandal, S., 2015. Evidence for a far-traveled thrust sheet in the Greater Himalayan thrust system, and an alternative model to building the Himalaya. Tectonics 34, 31–52.

Kohn M.J., 2004. Oscillatory- and sector-zoned garnets record cyclic (?) rapid thrusting in central Nepal. Geochemistry Geophysics Geosystems 5, Q12014.

Kohn, M.J., 2008. PTt data from central Nepal support critical taper and repudiate large-scale channel flow of the Greater Himalayan Sequence. Geological Society of America Bulletin 120, 259–273.

Kohn, M.J., Wieland, M.S., Parkinson, C.D. Upreti, B.N., 2004. Miocene faulting at plate tectonic velocity in the Himalaya of central Nepal. Earth and Planetary Science Letters 228, 299–310.

Kohn, M.J., Wielnand, M., Parkinson, C.D., Upreti, B.N., 2005. Five generation of monazite in Langtang gneisses: implication for chronology of the Himalayan metamorphic core. Journal of Metamorphic Geology 23, 399–406.

Kohn, M.J., Paul, S.K., Corrie, S.L., 2010. The lower Lesser Himalayan Sequence: A Paleoproterozoic arc on the northern margin of the Indian plate. Geological Society of America Bulletin 122, 323-335.

Kriegsman, L.M., lvarez-Valero, A.M., 2010. Melt-producing versus melt-consuming reactions in pelitic xenoliths and migmatites. Lithos 116, 310–320.

Larson, K.P., Cottle, J.M., 2014. Midcrustal discontinuities and the assembly of the Himalayan mid-crust. Tectonics 33, 718–740.

Larson, K.P., Godin, L., Price, R.A., 2010. Relationships between displacement and distortion in orogens: linking the Himalayan foreland and hinterland in central Nepal. Geological Society of America Bulletin 122, 1116–1134.

943 Larson, K.P., Gervais, F., Kellett, D.A., 2013. A P–T–t–D discontinuity in east-central
944 Nepal: Implications for the evolution of the Himalayan mid-crust. Lithos 179, 275–
945 292.
946 Larson, K.P., Ambrose, T.K., Webb, A.G., Cottle, J.M., Shrestha, S., 2015.
947 Reconciling Himalayan midcrustal discontinuities: the Main Central thrust system.
948 Earth and Planetary Science Letters 429, 139–146.
949 Law, R.D., Searle, M. P., Simpson, R.L., 2004. Strain, deformation temperatures and
950 vorticity of flow at the top of the Greater Himalayan Slab, Everest Massif, Tibet.
951 Journal of the Geological Society, London 161, 305–320.
952 Le Fort, P., Rai, S.M., 1999. Pre-Tertiary felsic magmatism of the Nepal Himalaya.
953 Recycling of continental crust. Journal of Asian Earth Sciences 17, 607 628.
954 Lombardo, B., Pertusati, P., Borghi, A., 1993. Geology and tectono-magmatic
955 evolution of the eastern Himalaya along the Chomolungma–Makalu transect. In:
956 Treloar, P.J., Searle, M.P. (Eds.), Himalayan Tectonics. Geological Society of
957 London Special Publication 74, 341–355.
958 Macfarlane, A.M., 1993. Chronology of tectonic events in the crystalline core of the
959 Himalaya, Langtang National Park, central Nepal. Tectonics 12, 1004–1025.
960 Macfarlane, A.M., 1995. An evaluation of the inverted metamorphic gradient at
961 Langtang National Park, Central Nepal, Himalaya. Journal of Metamorphic
962 Geology 13, 595–612.
963 Macfarlane, A.M., Hodges, K.V., Lux, D., 1992. A structural analysis of the Main
964 Central Thrust zone, Langtang National Park, central Nepal Himalaya. Geological
965 Society of America Bulletin 104, 1389–1402.
966 Martin, A.J., 2017. A review of definitions of the Himalayan Main Central Thrust.
967 International Journal of Earth Sciences 106, 2131-2145.

968 Martin, A.J., DeCelles, P.G., Gehrels, G.E., Patchett, P.J., Isachsen, C., 2005.
969 Isotopic and structural constraints on the location of the Main Central thrust in the
970 Annapurna Range, central Nepal Himalaya. Geological Society of America Bulletin
971 117, 926–944.
972 McQuarrie, N., Robinson, D.M., Long, S.P., Tobgay, T., Grujic, D., Gehrels, G.E.,
973 Ducea, M., 2008. Preliminary stratigraphic and structural architecture of Bhutan:
974 implications for the along strike architecture of the Himalayan system. Earth and
975 Planetary Science Letters 272, 105–117.
976 Montomoli, C., Iaccarino, S., Carosi, R., Langone, A., Visonà, D., 2013.
977 Tectonometamorphic discontinuities within the Greater Himalayan Sequence in
978 Western Nepal (Central Himalaya): Insights on the exhumation of crystalline rocks.
979 Tectonophysics 608, 1349–1370.
980 Montomoli, C., Carosi, R., Iaccarino, S., 2015. Tectonometamorphic discontinuities in
981 the Greater Himalayan Sequence: a local or a regional feature? Geological
982 Society London Special Publications 412, 25–41.
983 Mosca, P., Groppo, C., Rolfo, F., 2012. Structural and metamorphic features of the
984 Main Central Thrust Zone and its contiguous domains in the eastern Nepalese
985 Himalaya. Journal of Virtual Explorer, Electronic Edition 41, paper 2.
986 Newton, R.C., Charlu, T.V., Kleppa, O.J., 1980. Thermochemistry of the high
987 structural state Pls. Geochimica et Cosmochimica Acta 44, 933–941.
988 Pearson, O.N., 2002. Structural evolution of the central Nepal fold-thrust belt and
989 regional tectonic and structural significance of the Ramgarh thrust. Ph.D.,
990 University of Arizona.

991 Pearson, O.N., DeCelles, P.G., 2005. Structural geology and regional tectonic
992 significance of the Ramgarh Thrust, Himalayan fold-thrust belt of Nepal. Tectonics
993 24, TC4008.
994 Pognante, U., Benna, P., 1993. Metamorphic zonation, migmatization, and
995 leucogranites along the Everest transect (eastern Nepal and Tibet): record of an
996 exhumation history. In: Treloar, P.J., Searle, M.P. (Eds.), Himalayan Tectonics.
997 Geological Society of London Special Publications 74, 323-340.
998 Pouchou, J.L., Pichoir, F., 1988. Determination of mass absorption coefficients for
999 soft X-rays by use of the electron microprobe. In: Newbury, D.E. (Eds.),
1000 Microbeam Analysis. San Francisco, CA: San Francisco Press, pp. 319-324.
1001 Powell, R., Holland, T.J.B., 1994. Optimal geothermometry and geobarometry.
1002 American Mineralogist 79, 120-133.
1003 Rapa, G., Groppo, C., Mosca, P., Rolfo, F., 2016. Petrological constraints on the
1004 tectonic setting of the Kathmandu Nappe in the Langtang-Gosainkund-Helambu
1005 regions, Central Nepal Himalaya. Journal of Metamorphic Geology 34, 999–1023.
1006 Rapa, G., Groppo, C., Rolfo, F., Petrelli, M., Mosca, P., Perugini, D., 2017. Titanite-
1007 bearing calc-silicate rocks constrain timing, duration and magnitude of metamorphic
1008 CO_2 degassing in the Himalayan belt. Lithos 292-293, 364-378.
1009 Reddy, S.M., Searle, M.P., Massey, J.A., 1993. Structural evolution of the High
1010 Himalayan gneiss sequence, Langtang Valley, Nepal. In: Treloar, P.J., Searle,
1011 M.P., (Eds.), Himalayan Tectonics. Geological Society of London Special
1012 Publications 74, 375–389.
1013 Richards, A., Argles, T., Harris, N., Parrish, R., Ahmad, T., Darbyshire, F., Draganits,
1014 E., 2005. Himalayan architecture constrained by isotopic tracers from clastic
1015 sediments. Earth and Planetary Science Letters 236, 773–796.

1016 Robinson, D.M., DeCelles, P.G., Patchett, P.J., Garzione, C.N., 2001. The kinematic
1017 evolution of the Nepalese Himalaya interpreted from Nd isotopes. Earth and
1018 Planetary Science Letters 192, 507–521.
1019 Robinson, D.M., DeCelles, P.G., Copeland, P., 2006. Tectonic evolution of the
1020 Himalayan thrust belt in western Nepal: implications for channel flow models.
1021 Geological Society of American Bulletin 118, 865–885.
1022 Rolfo, F., Groppo, C., Mosca, P., 2015. Petrological constraints of the “Channel Flow”
1023 model in eastern Nepal. In: Mukherjee, S., Carosi, R., van der Beek, P.A.,
1024 Mukherjee, B.K., Robinson, D.M. (Eds.), Tectonics of the Himalaya. Geological
1025 Society of London Special Publications 412, 177–197.
1026 Rubatto, D., Chakraborty, S., Dasgupta, S., 2013. Timescales of crustal melting in
1027 the Higher Himalayan Crystallines (Sikkim, Eastern Himalaya) inferred from trace
1028 element-constrained monazite and zircon chronology. Contribution to Mineralogy
1029 and Petrology 165, 349-372.
1030 Searle, M.P., Law, R.D., Godin, L., Larson, K.P., Streule, M.J., Cottle, J.M., Jessup,
1031 M.J., 2008. Defining the Himalayan Main Central Thrust in Nepal. Journal of the
1032 Geological Society of London 165, 523–534.
1033 Schelling, D., 1992. The tectonostratigraphy and structure of the eastern Nepal
1034 Himalaya. Tectonics 11, 925–943.
1035 Schelling, D., Arita, K., 1991. Thrust tectonics, crustal shortening, and the structure of
1036 the far-eastern Nepal, Himalaya. Tectonics 10, 851–862.
1037 Stocklin, J., 1980. Geology of Nepal and its regional frame. Journal of the Geological
1038 Society of London 137, 1-34.

1039 Tajčmanová, L., Connolly, J.A.D., Cesare, B., 2009. A thermodynamic model for
1040 titanium and ferric iron solution in biotite. Journal of Metamorphic Geology 27,153–
1041 165.
1042 Takagi, H., Arita, K., Sawaguchi, T., Kobayashi, K., Awaji, D., 2003. Kinematic history
1043 of the Main Central Thrust zone in the Langtang area, Nepal. Tectonophysics 366,
1044 151–163.
1045 Thompson, J.B., Hovis, G.L., 1979. Entropy of mixing in sanidine. American
1046 Mineralogist 64, 57–65.
1047 Upreti, B. N., 1999. An overview of the stratigraphy and tectonics of the Nepal
1048 Himalaya. Journal of Asian Earth Sciences 17, 577–606.
1049 Wang, J. M., Zhang, J. J., Wang, X.X., 2013. Structural kinematics, metamorphic P–
1050 T profiles and zircon geochronology across the Greater Himalayan Crystalline
1051 Complex in south-central Tibet: implication for a revised channel flow. Journal of
1052 Metamorphic Geology 31, 607–628.
1053 Wang, J-M., Zhang, J-J., Liu, K., Wang, X-X., Rai, S., Scheltens, M., 2016. Spatial
1054 and temporal evolution of tectonometamorphic discontinuities in the Central
1055 Himalaya: Constraints from P-T paths and geochronology. Tectonophysics 679,
1056 41-60.
1057 Waters, D.J., 2001. The significance of prograde and retrograde quartz-bearing
1058 intergrowth microstructures in partially melted granulite-facies rocks. Lithos 56,
1059 97–110.
1060 White, R.W., Powell, R., Holland, T.J.B., 2001. Calculation of partial melting equilibria
1061 in the system Na_2O-CaO-K_2O-FeO-MgO-Al_2O_3-SiO_2-H_2O (NCKFMASH). Journal
1062 of Metamorphic Geology 19, 139–153.

White, R.W., Powell, R., Holland, T.J.B., 2007. Progress relating to calculation of partial melting equilibria for metapelites. Journal of Metamorphic Geology 25, 511–527.

Whitney, D.L., Evans, B.W., 2010. Abbreviations for names of rock-forming minerals. American Mineralogist 95, 185–187.

Yakymchuk, C., Godin, L., 2012. Coupled role of deformation and metamorphism in the construction of inverted metamorphic sequences: an example from far-northwest Nepal. Journal of Metamorphic Geology 30, 513–535.

CAPTIONS

Fig. 1 – Simplified geological map of central-eastern Himalaya, with major tectonometamorphic units (modified from Goscombe and Hand, 2000, He et al., 2015,Wang et al., 2016 and based on our own data). Traces for the three transects studied in this paper are reported (G: Gatlang; L: Langtang; GH: Gosainkund-Helambu). 1: Siwalik deposits; 2: Lesser Himalayan Sequence; 3: Lower Greater Himalayan Sequence; 4: Upper Greater Himalayan Sequence; 5: Tethyan Sedimentary Sequence (dark: Ordovician-Mesozoic; Light: Precambrian-Cambrian). MFT: Main Frontal Thrust; MBT: Main Boundary Thrust; MCT: Main Central Thrust; STDS: South Tibetan Detachment System. The study area is located in the white rectangle, and reported in Fig. 2.

Fig. 2 – Geological map of the investigated area, with equal area stereo plots of representative structural data. LT, Langtang Thrust; MCT, Main Central Thrust; RT, Ramgarh Thrust; LHS, Lesser Himalayan Sequence; L-GHS, Lower Greater Himalayan Sequence; U-GHS, Upper Greater Himalayan Sequence.

Fig. 3 – Representative LHS and LHS-Ramgarh Thrust Sheet lithologies at the meso- and microscale. (a,b) Graphite-rich two-mica phyllite with porphyroblastic garnet from the LHS. Garnet is partially wrapped around by the $S_{2(LHS)}$ foliation defined by the alignment of Bt + Wm + Gr; its rim, however, overgrows the $S_{2(LHS)}$ foliation. Note the rotated internal schistosity in Grt (b: Plane Polarized Light, PPL). (c,d) Quartzites from the LHS-Ramgarh Thrust Sheet. In (c), quartzites (bottom) are in contact with phyllitic schists (top). Quartzites are strongly foliated, with the main $S_{2(L\text{-}GHS)}$ foliation defined by Bt + Wm + St alignment (d: PPL). (e, f) Two-mica augen

gneiss from the LHS-Ramgarh Thrust Sheet, showing a well-developed mylonitic fabric defined by Wm + Bt. (f: Crossed Polarized Light, XPL).

Fig. 4 –Representative meso- and micro-structures of the LHS and LHS-Ramgarh Thrust Sheet lithologies. (a) Mesoscopic shear zones developed during the $D_{2(LHS)}$ phase, leading to the progressive parallelization of the $S_{1(LHS)}$ and $S_{2(LHS)}$ foliations. (b) Mica-fish showing top-to-the-south sense of shear. (c) $S_{2(LHS)}$ foliation folded and crenulated by $D_{3(LHS)}$ phase. (d) Mesoscopic relationships between the $L_{2(LHS)}$ and $Lcr_{3(LHS)}$. (e,f) Late top-to-the-north extensional structures in the LHS lithologies.

Fig. 5 – Representative Lower-GHS (L-GHS) lithologies at the meso- and microscale. (a) Compositional layering in two-micas + Grt metapelites, with bands parallel to the $S_{2(L\text{-}GHS)}$ schistosity. (b) Kyanite porphyroblasts are elongated parallel to the $S_{2(L\text{-}GHS)}$ and define a stretching lineation. $S_{2(L\text{-}GHS)}$ schistosity is indicated. (c) Layers of micaschists with variable thickness intercalated in fine-grained gneisses. (d) Detail of a melt-related microstructure (melt pseudomorph) in a Lower-GHS sample from the uppermost structural levels (PPL). (e) Boudin of a Cpx + Pl ± Grt ± Scp ± Kfs ± Cal calc-silicate rock, outcropping in the Helambu region. (f) Banded quartzites from the lowermost structural levels of the Lower-GHS (Gatlang region).

Fig. 6 – Representative mesostructures of Lower-GHS (L-GHS) lithologies. (a) Relationships between $S_{2(L\text{-}GHS)}$ and $S_{3(L\text{-}GHS)}$ schistosities. (b-d) Deformation structures related to the $D_{3(L\text{-}GHS)}$ event, leading to pervasive stretching and boudinage.

Fig. 7 – Representative lithologies and mesostructures of Upper-GHS (U-GHS). (a) Migmatitic paragneiss with leucosomes parallel to the $S_{m(U\text{-}GHS)}$. (b) Detail of a Grt + Sil gneiss, with garnet porphyroblasts surrounded by a plagioclase corona. (d) Layers of calc-silicate rocks (Cpx + Kfs + Scp ± Pl ± Qz ± Cal), variably deformed. (d) Metre thick layer of fine-grained biotitic gneiss with Sil-rich nodules, intercalated within migmatitic orthogneisses. (e) Strongly mylonitic migmatitic paragneiss in the Gatlang region, with leucosomes elongated parallel to the main foliation. (f) Shear zone with top-to-the-south movement in the mylonitic migmatitic gneisses.

Fig. 8 – Representative microstructures of the studied samples. (a) Sample 15-19. The main $S_{2(LHS)}$ foliation is defined by Bt + Wm, while skeletal Grt preserves an internal rotated foliation (inset). (PPL, inset: XPL). (b,c) Sample 15-28b. Porphyroblastic Grt has an internal foliation which is continuous with the external $S_{2(LHS)}$ foliation, defined by Wm + Bt (PPL). Ky occur as inclusions in Grt rims (b) and in the matrix (c), and St is included in Grt rim (c). The inset in (c) shows $S_{1(LHS)}$ preserved in a microlithon (PPL). (d,e) Sample 15-26b. Grt porphyroblasts are partly wrapped by the $S_{2(LHS)}$ foliation, and Grt rims show straight equilibrium contacts with both Bt and Wm. The inset shows the $S_{2(LHS)}$ foliation defined by Bt + Wm. (e). Grt includes Qz, Bt, Wm, Rt, Ilm and Pl (not shown) (d: PPL, inset: XPL; e:BSE). (f,g) Sample15-38. Large Grt porhyroblasts (bottom left) are partly wrapped by the main $S_{2(L\text{-}GHS)}$ foliation, defined by Bt + Wm alignment (inset) (PPL, inset: XPL). In (g) St in the matrix includes Rt, Qz and Pl and Ky is replaced by Wm (PPL). (h,i) Sample 14-12. In (h) the compositional banding is defined by Bt + Sil mesocratic domains, alternating with Qz + Pl + Kfs ± Bt leucocratic domains (PPL). Wm locally replaces Sil. In (i) skeletal Grt is replaced by a Pl corona, and includes Bt, Pl and Qz (XPL).

Fig. 9 – P-T conditions obtained using the Average PT approach applied to LHS and GHS metapelite samples. (a, b) LHS samples: prograde and peak P-T conditions with uncertainties (a) and P-T evolutions inferred basing on AvPT results (arrows, b). (c, d) GHS samples from the Gatlang-Langtang transects: prograde and peak P-T conditions with uncertainties (c) and P-T evolutions inferred basing on AvPT results (arrows, d). (e, f) GHS samples from the Gosainkund-Helambu transect: peak P-T conditions with uncertainties. Light grey and dark grey fields are the Wm and Bt dehydration melting fields respectively, separated by the H_2O-saturated *solidus* and the Wm–out reaction (modified from White et al., 2001).

Fig. 10 – (a, b) Estimated peak temperature (a) and pressure (b) conditions, reported from left to right from lower to upper structural levels. The x-axis is not to scale. T and P results constrained using the Average PT method (circles) are compared to results obtained using pseudosections (squares) (derived from Rapa et al., 2016, except for sample 15-26b which has been modelled in this study). The lines (and coloured boxes) refer to the weighted mean values (and errors) obtained with the pseudosection approach; the dashed lines (and dashed boxes) refer to the weighted mean values (and errors) obtained with the Average PT method; the dotted lines (and dotted boxes) refer to the weighted mean values (and errors) obtained for the Kohn (2008) samples, calculated using the conventional thermobarometry approach. (c) T/P ratios (°C/kbar) (with errors) plotted as a function of the (approximate) structural position for the samples studied in this work (sample 15-26b) and in Rapa et al. (2016). The lines (and coloured boxes) refer to the weighted mean values (and errors) obtained with the pseudosection approach; the dashed lines (and dashed

boxes) refer to the weighted mean values (and errors) obtained with the Average PT method; the dotted lines (and dotted boxes) refer to the weighted mean values (and errors) obtained for the Kohn (2008) samples, calculated using the conventional thermobarometry approach.

Fig. 11 – *P–T* pseudosection for sample 15-26b (LHS-Ramgarh Thrust Sheet, Gatlang transect) calculated in the MnNCKFMASTH system at $a(H_2O)=1$. Unfractionated and fractionated (*) bulk-rock compositions are given in mol%. (a) *P–T* pseudosection calculated using the unfractionated bulk composition, used to model the *P–T* conditions for the growth of Grt core. In (a–c), di– tri, quadri–, quini–, esa– and epta– variant fields are represented in different grey tones, from white (di-variant) to the darker grey (epta-variant). Ms and Pg refer to K–rich and Na–rich white micas, respectively. The white dotted rectangle in (a) refers to the *P–T* interval shown in (b), (c) and (d). (b) Detail of (a) with compositional isopleths of Grt core. (c) *P–T* pseudosection calculated using the fractionated bulk composition, used to model the *P-T* conditions for the growth of Grt rim, contoured for Grt rim composition. The white dashed polygon in (b) and (c) constrain the *P–T* conditions inferred for the growth of Grt core and rim, respectively. (d) *P–T* path inferred for sample 15-26b basing on mineral assemblages and compositions (light purple arrow). The dashed lines (melt-in) in (a) to (d) are the H_2O-saturated solidus.

Fig. 12 – P–T diagrams showing the P–T trajectories obtained for the studied metapelites from the Gatlang-Langtang (a,c) and Gosainkund–Helambu (b,d) transects using the pseudosection (a,b) and AvPT (c,d) approaches (Rapa et al., 2016 and this study). Asterisks in (a,b) indicate data from Rapa et al. (2016). Light

1198 grey and dark grey fields represent Wm and Bt dehydration melting fields,
1199 respectively, separated by the H_2O-saturated solidus and the Wm–out reaction
1200 (modified from White et al., 2001).

Figure 1

Click here to download high resolution image

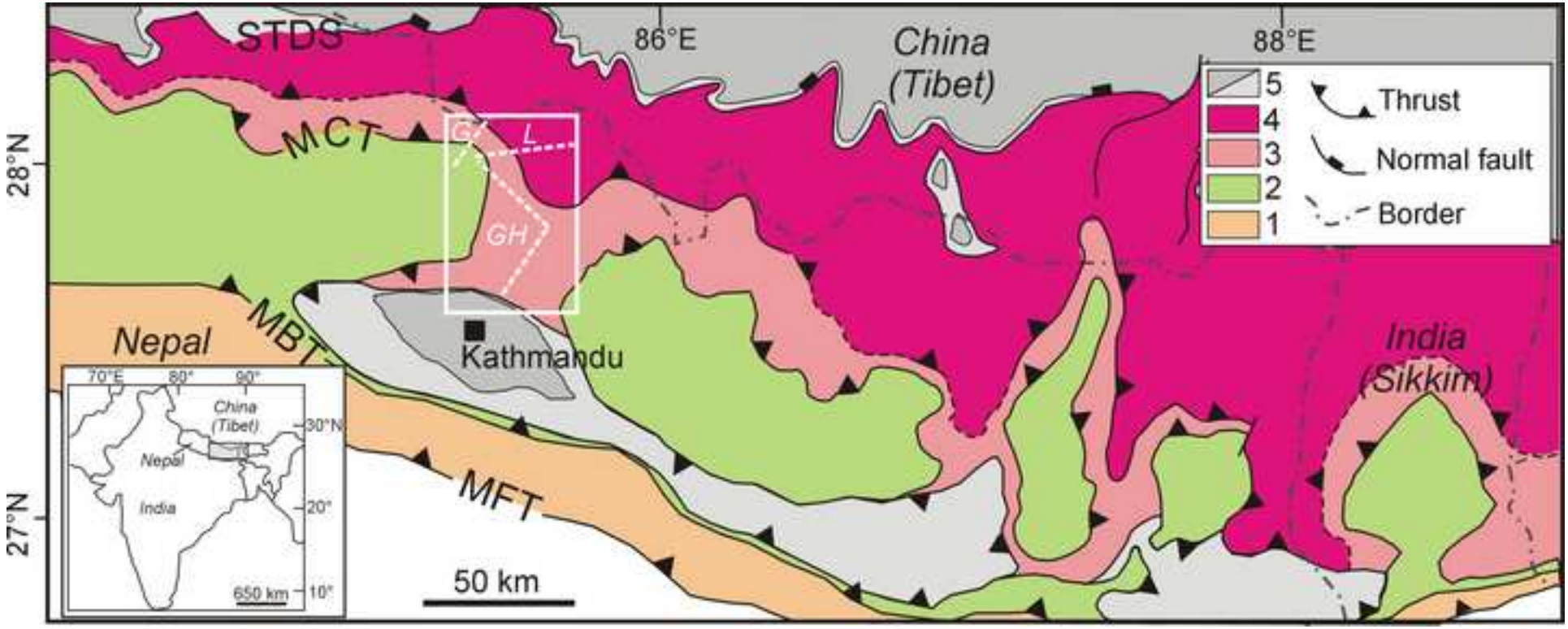

Figure 2

Click here to download high resolution image

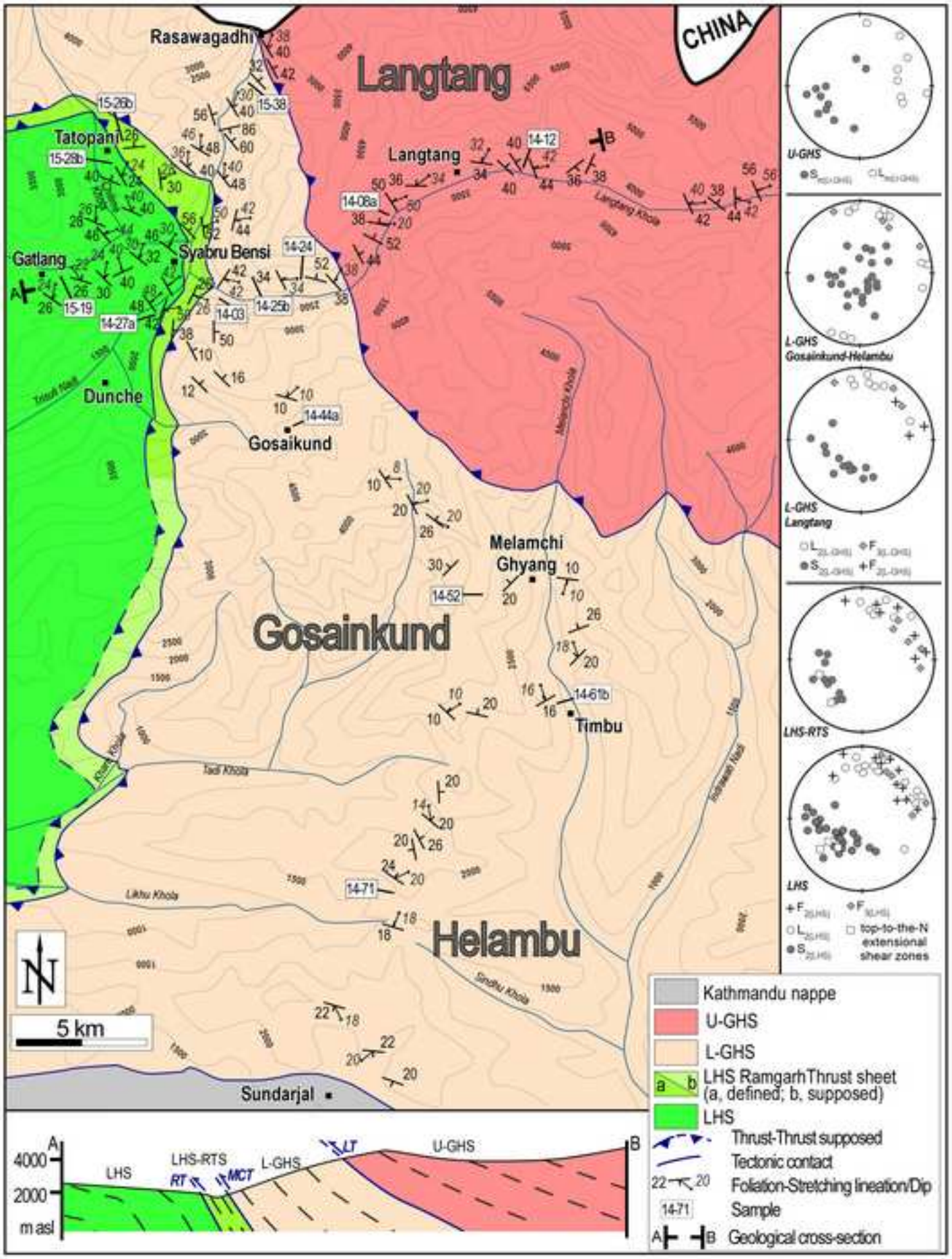

Figure 3

Click here to download high resolution image

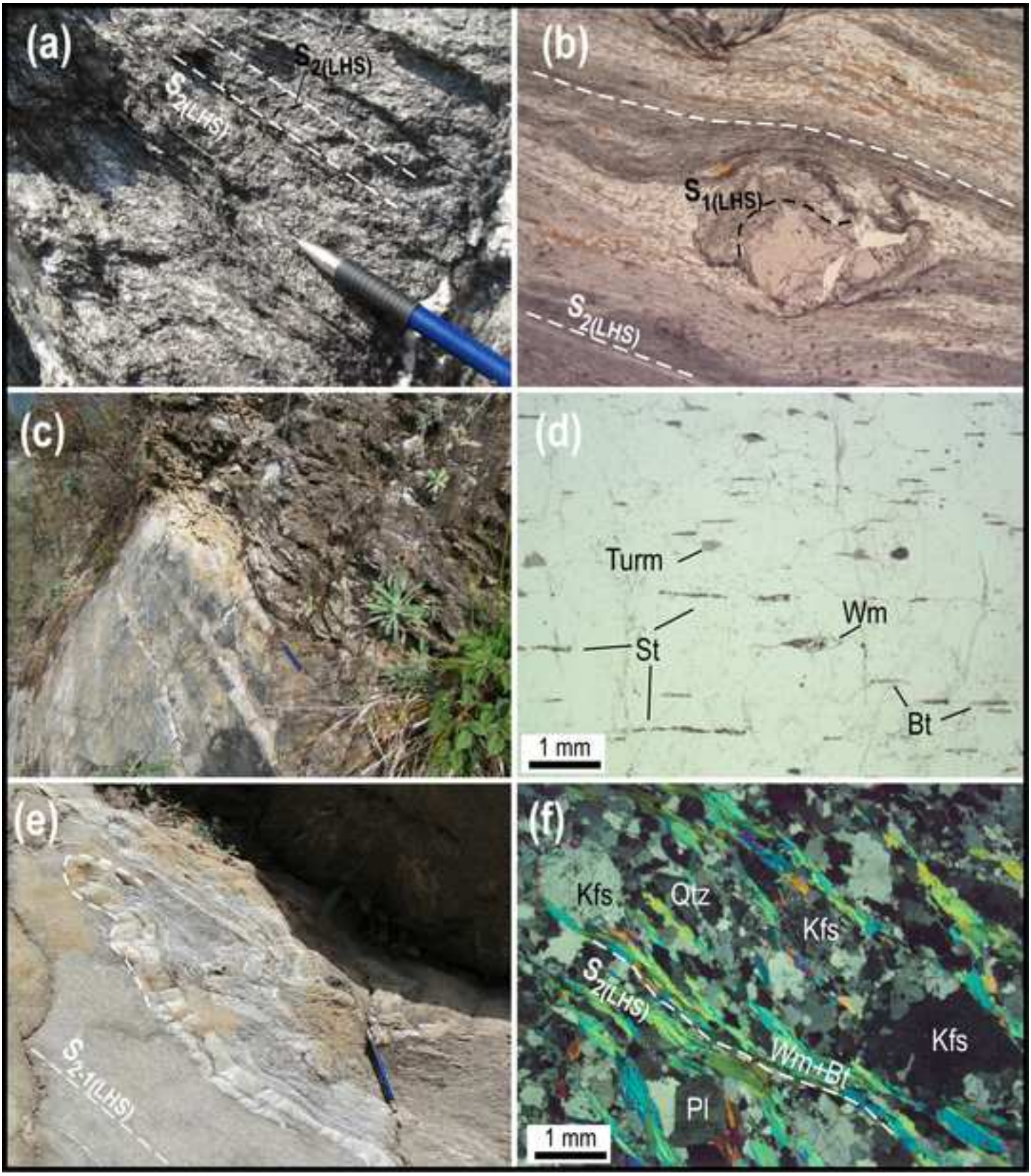

Figure 4

Click here to download high resolution image

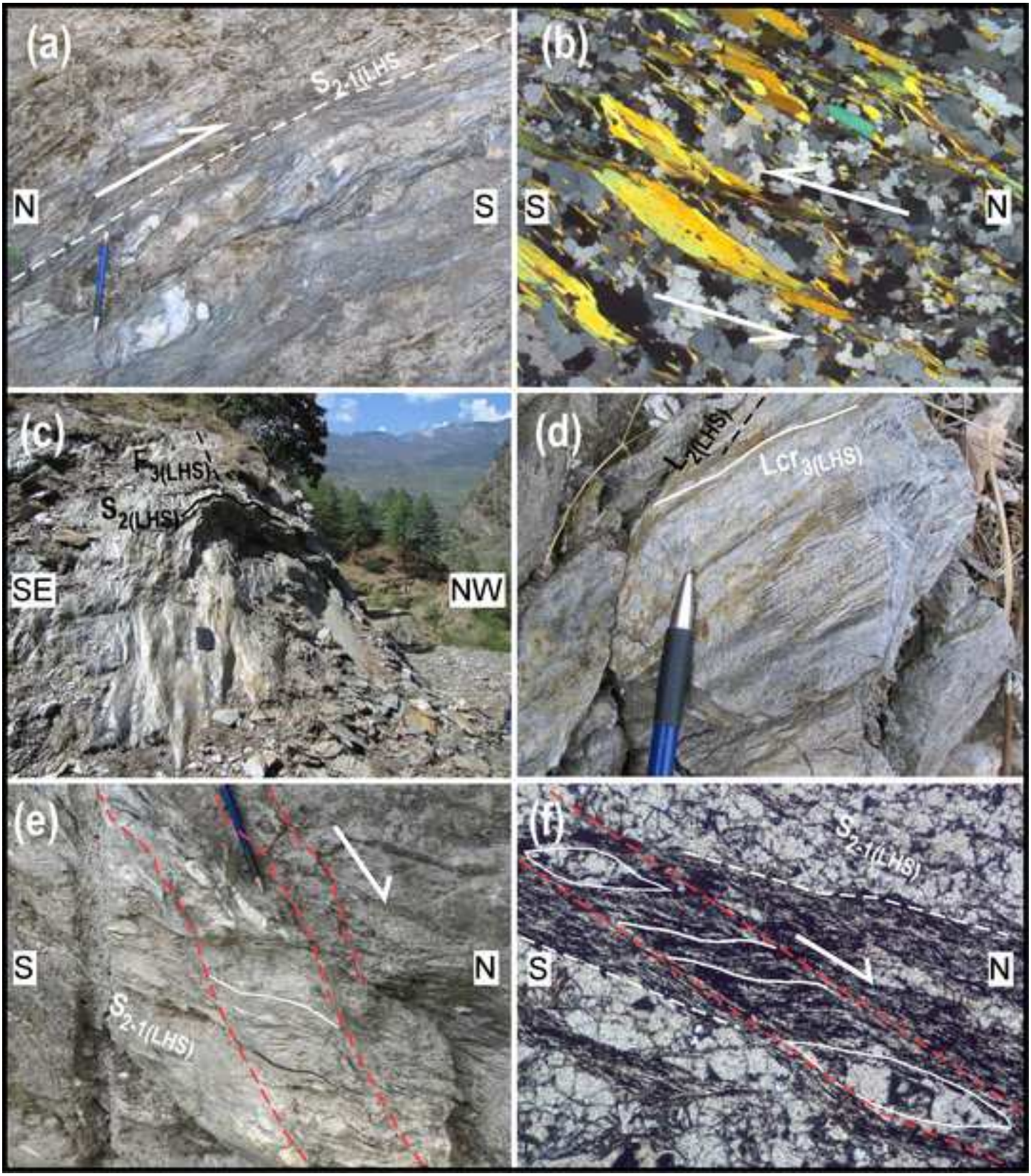

Figure 5

Click here to download high resolution image

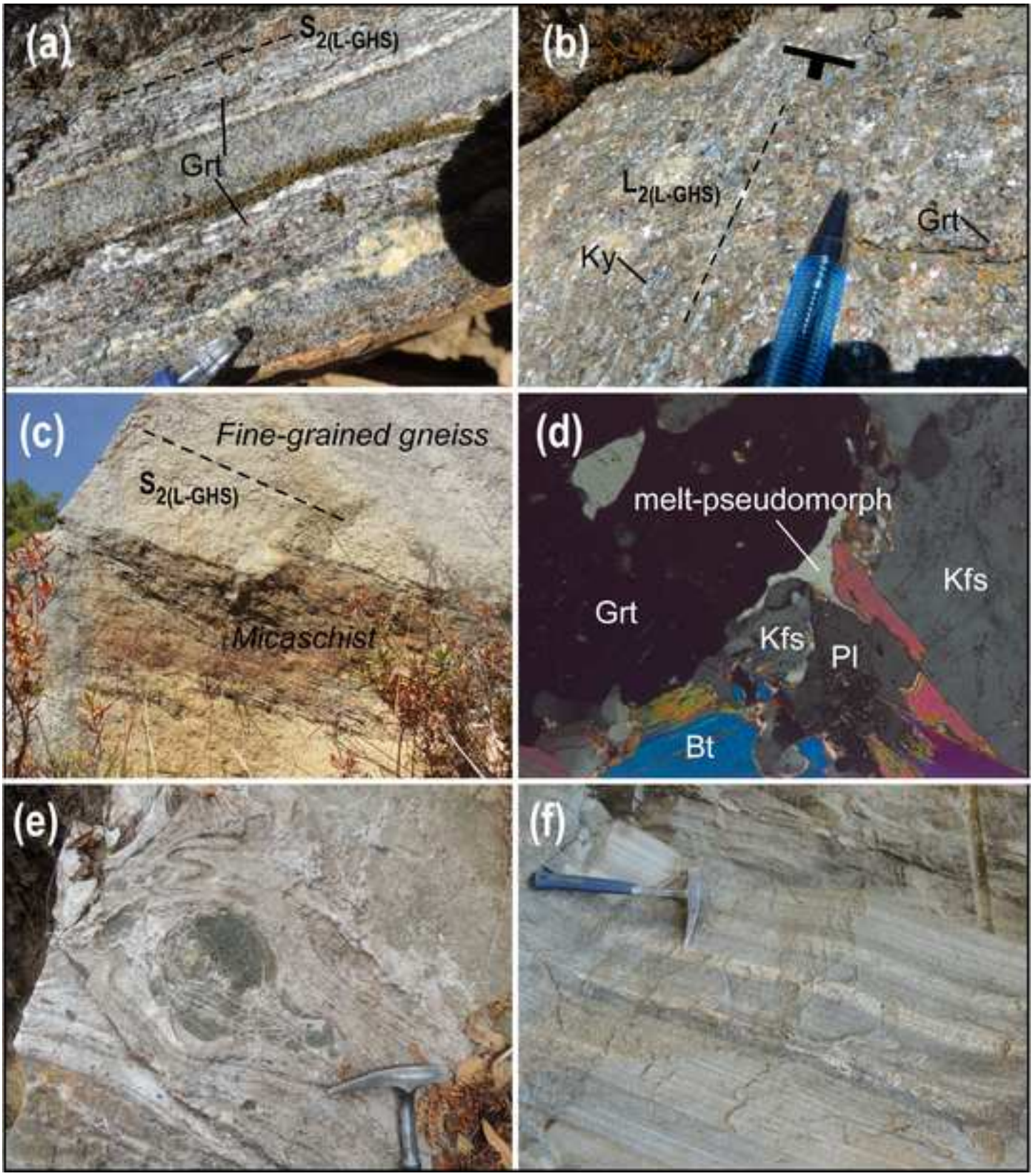

Figure 6

Click here to download high resolution image

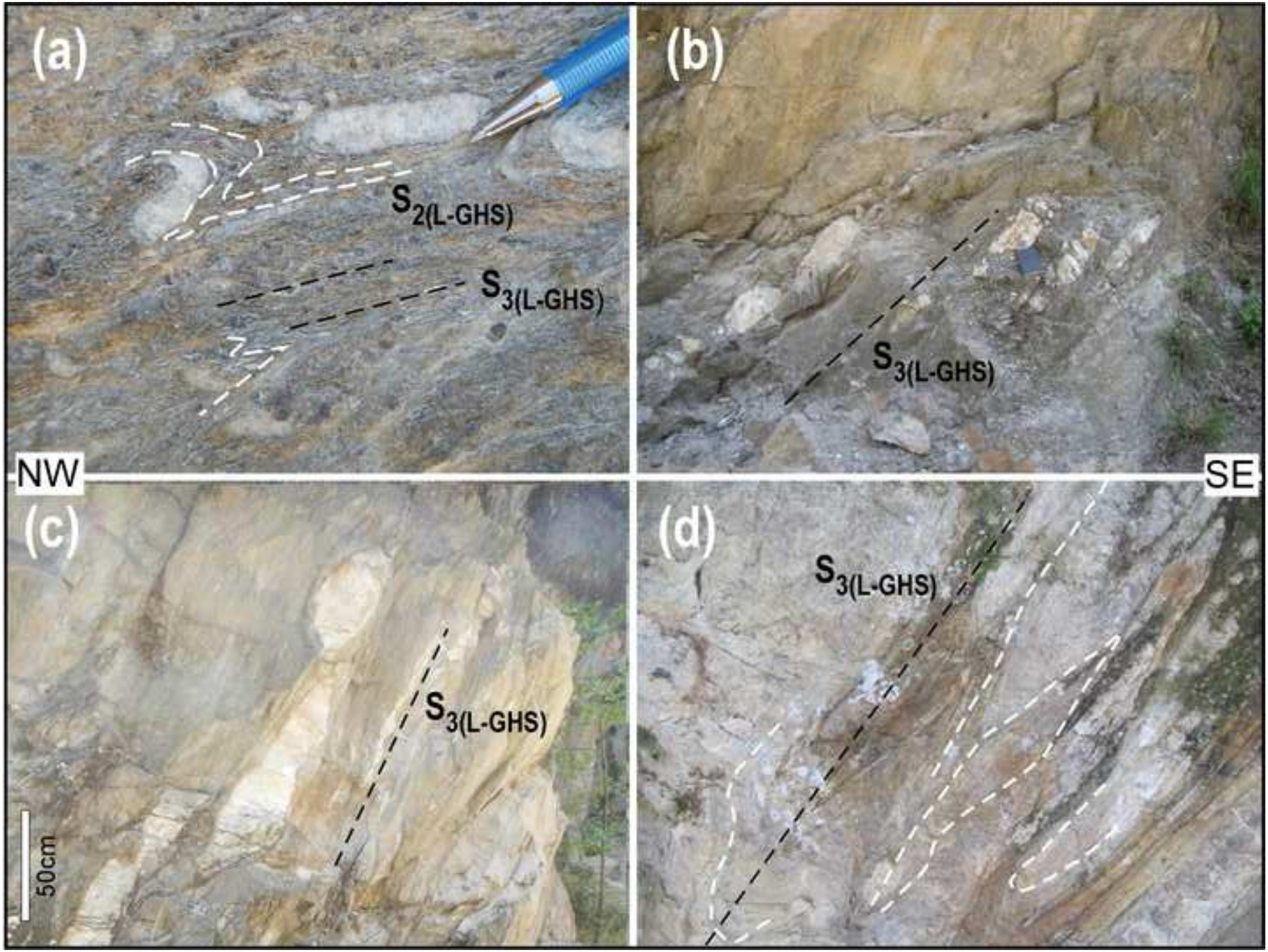

Figure 7

Click here to download high resolution image

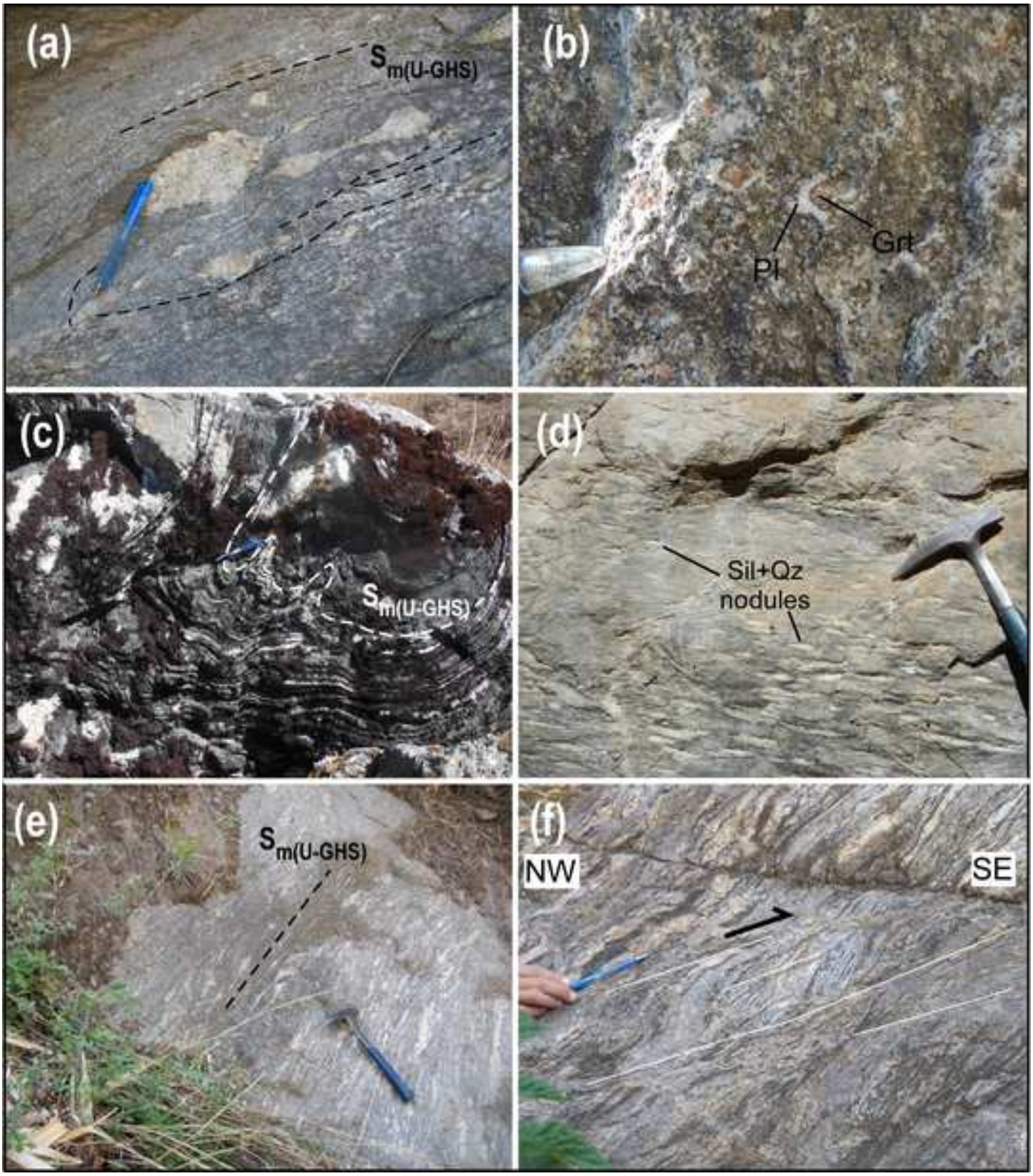

Figure 8

Click here to download high resolution image

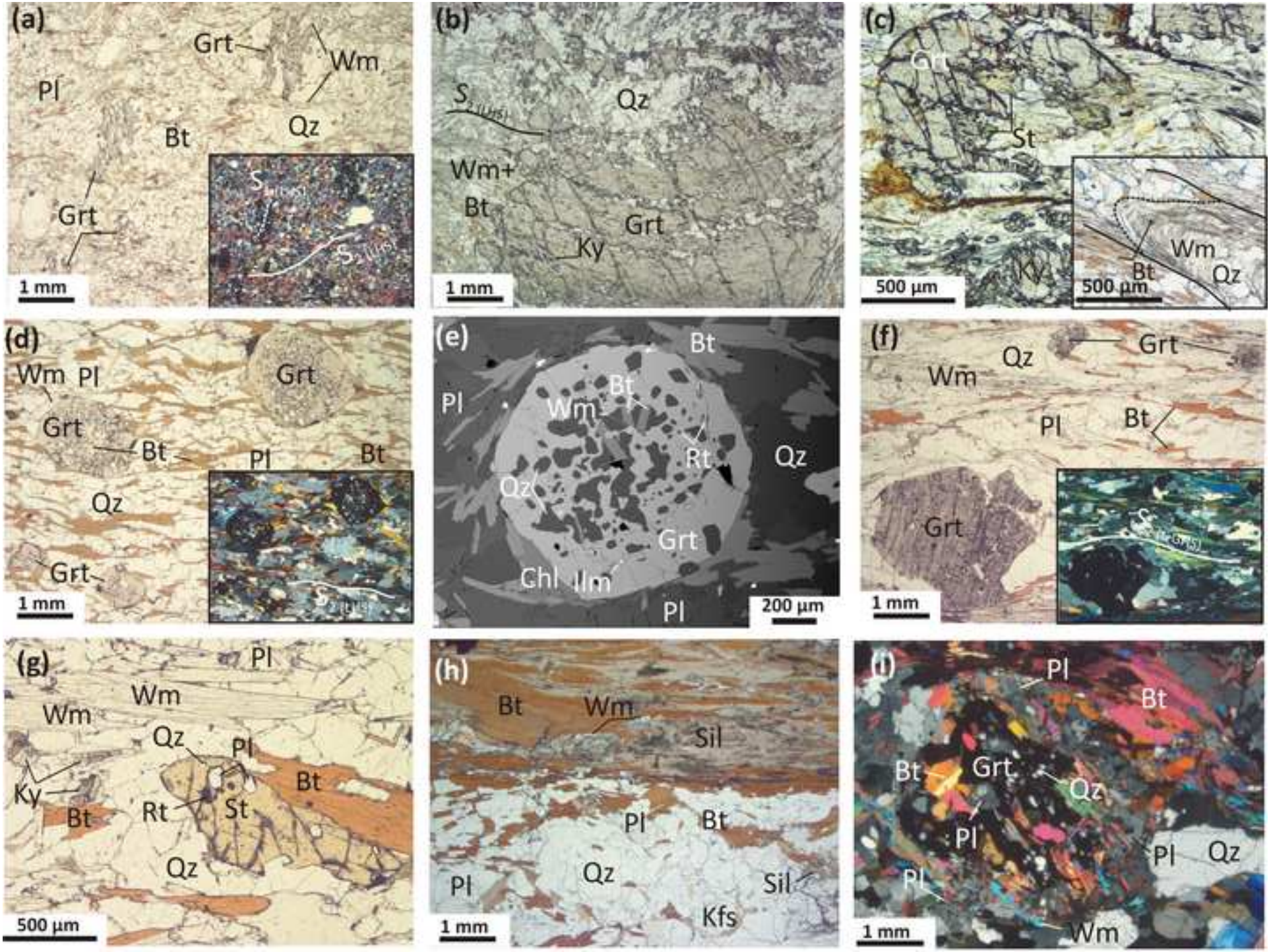

Figure 9

Click here to download high resolution image

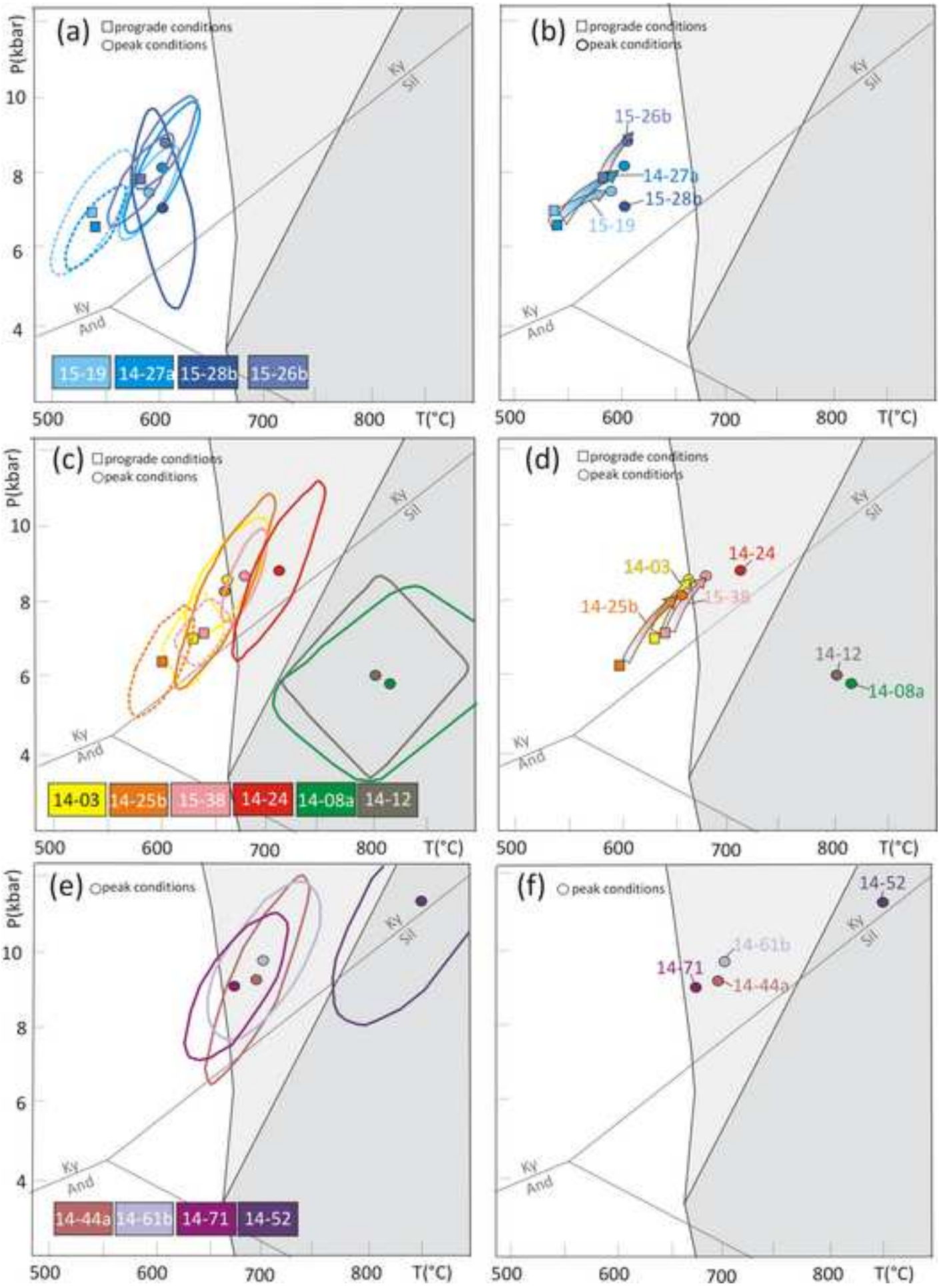

Figure 10

Click here to download high resolution image

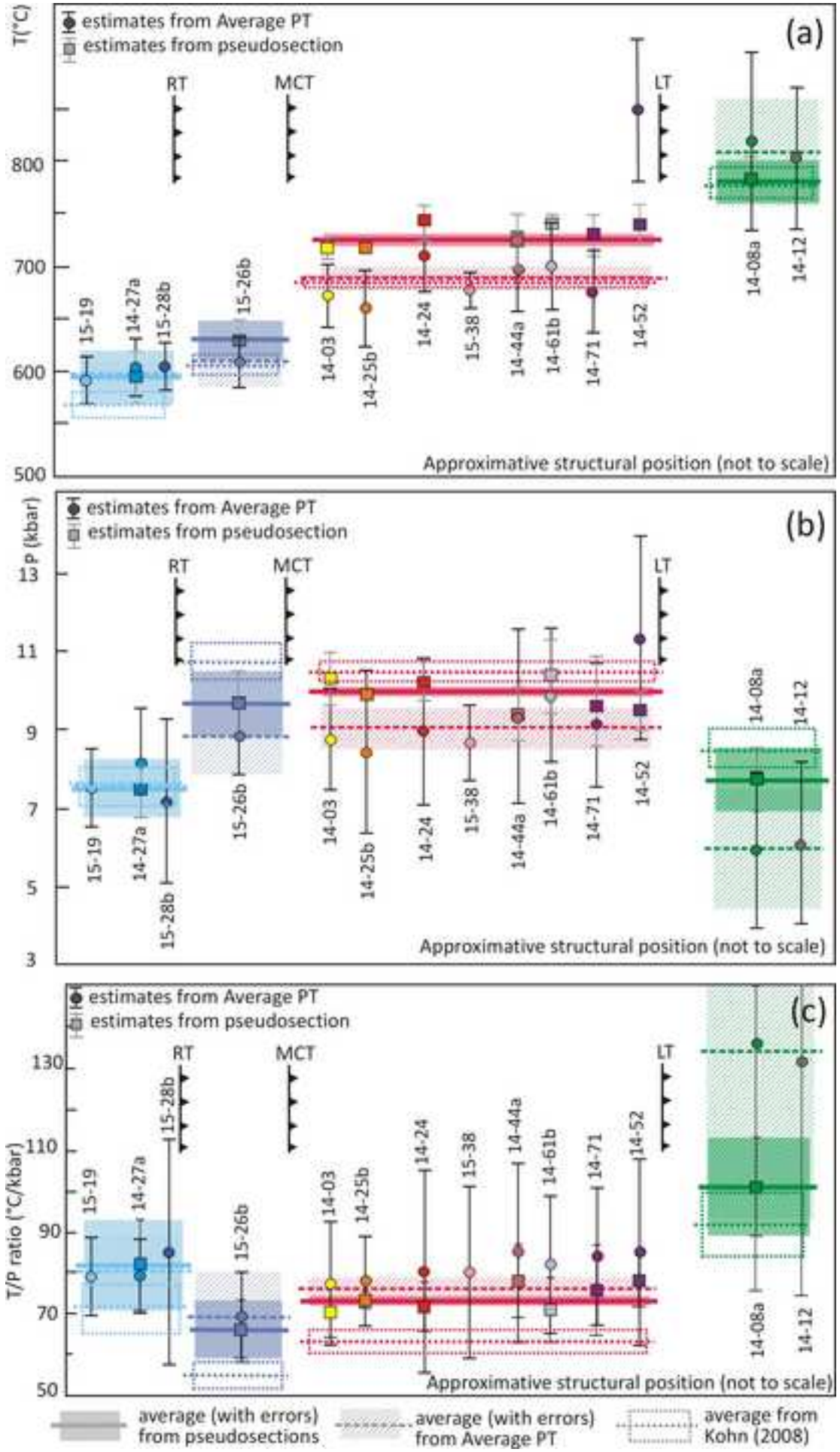

Figure 11

Click here to download high resolution image

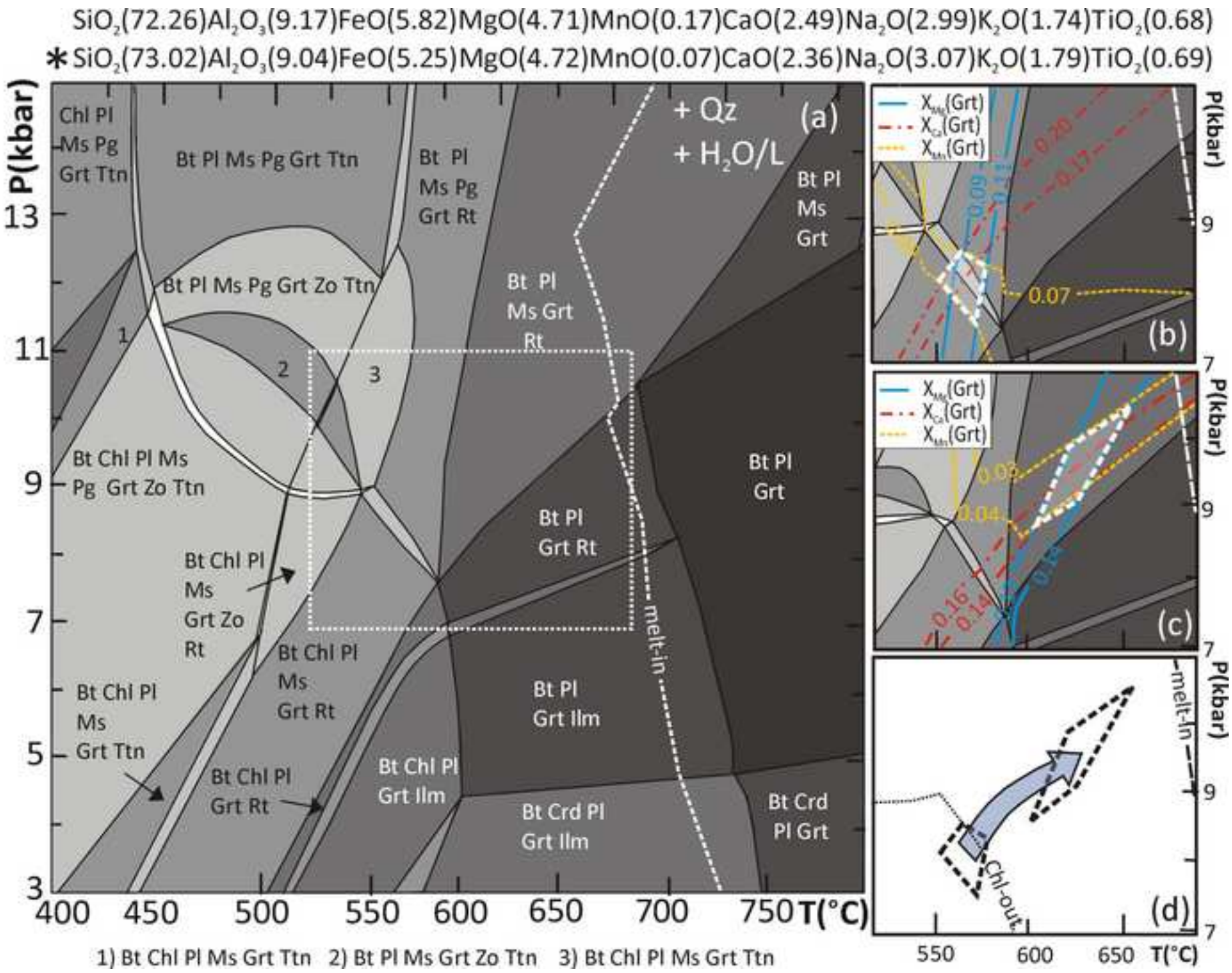

Figure 12

Click here to download high resolution image

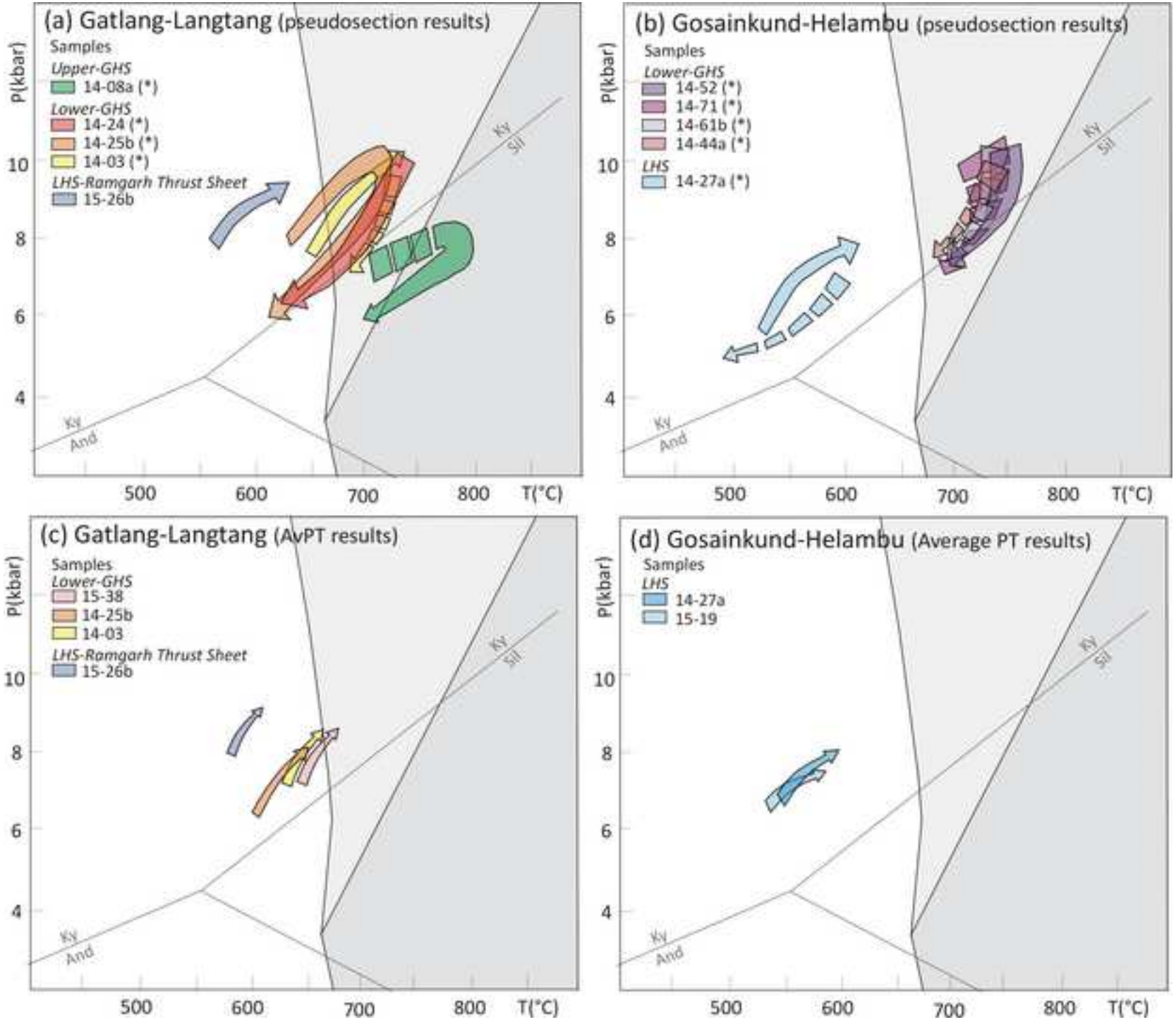

Table 1

Table 1 - Microstructural features of metapelites from Rapa et al. (2016)

	Sample		Main assemblage	Accessories	Comments
LHS	**14-27a**	Two-mica graphitic phyllite, with porphyroblastic Grt	Qz, Pl, Wm, Bt, Chl, Grt	Ep, Gr, Tur, Op	$S_{1(LHS)}$: Chl + Bt + Wm + Pl + Ilm; $S_{2(LHS)}$: Bt + Wm + Gr. Grt is partly wrapped by $S_{2(LHS)}$ and includes rotated internal foliation defined by Qz + Chl + Ilm + Gr. Late Bt, Chl and Wm overgrow $S_{2(LHS)}$.
L-GHS	**14-03**	Wm + Bt + Grt micaschist	Qz, Pl, Wm, Bt, Grt, <<Sil	Rt, Ilm, Tur	$S_{2(L-GHS)}$: Wm + Bt. Grt core is crowded with inclusions (Qz + Bt + Chl + Rt + Ilm), whereas Grt rim is inclusion-free. Transition from Grt core to Grt rim is marked by nanogranites. Sil occurs at Grt and Wm rims.
	14-25b	Wm + Bt + Grt + Ky + St micaschist	Qz, Pl, Wm, Bt, Grt, Ky, St, <<Sil	Rt, Ilm, Tur	$S_{2(L-GHS)}$: Wm + Bt. Grt core is crowded with inclusions (Qz + Bt + Ilm), whereas Grt rim is inclusion-free. Transition from Grt core to Grt rim is marked by nanogranites. Ky is either in equilibrium with $S_{2(L-GHS)}$ or overgrows it. St overgrow $S_{2(L-GHS)}$ and replaces Ky. Sil occurs at Grt rims. Wm flakes overgows $S_{2(L-GHS)}$.
	14-24	Wm + Bt + Grt + Ky gneissic micaschist	Qz, Pl, Wm, Bt, Grt, Ky, St, <<Sil	Rt, Ilm, Tur	$S_{2(L-GHS)}$: Wm + Bt. Grt core is crowded with inclusions (Qz + Bt + Pl + Wm + Rt + Ilm), whereas Grt rim is inclusion-free. Transition from Grt core to Grt rim is marked by nanogranites. Ky is either in equilibrium with $S_{2(L-GHS)}$ or overgrows it. Sil occurs at Grt rims. Wm flakes overgow $S_{2(L-GHS)}$.
	14-44a	Wm + Bt + Ky micaschist, with porphyroblastic Grt	Qz, Pl, Bt, Wm, Grt, Ky	Rt, Ilm, Gr	$S_{2(L-GHS)}$: Wm + Bt + Gr. Grt core is crowded with inclusions, Grt rim is inclusion-free. Transition from Grt core to Grt rim is marked by nanogranites. Ky is rare. Wm flakes overgow $S_{2(L-GHS)}$.
	14-61b	Bt + Wm micaschist, with porphyroblastic Grt	Qz, Pl, Kfs, Bt, Wm, Grt	Ilm	$S_{2(L-GHS)}$: Bt + <Wm. Grt porphyroblasts are wrapped by it; they include Qz + Bt + Wm + Ilm. Grt is locally peritectic and includes Wm + Pl + Qz. Kfs is replaced by Pl. Pl is locally anti-perthitic. Wm flakes overgows $S_{2(L-GHS)}$.
	14-71	Bt + Wm + Grt + Sil gneissic micaschist	Qz, Pl, Bt, Wm, Grt, Sil	Ilm	$S_{2(L-GHS)}$: Bt + Wm. Grt core is crowded with inclusions (Qz + Pl + Bt Ilm), whereas Grt rim is inclusion-free. Transition from Grt core to Grt rim is marked by nanogranites. Late Wm flakes overgrow $S_{2(L-GHS)}$ and include Sil. Wm flakes overgow $S_{2(L-GHS)}$.
	14-52	Bt + Sil + Ky fine-grained gneiss, with porphyroblastic Grt	Qz, Pl, Bt, <<Wm, Grt, Sil, <Ky	Ilm	Banded structure, defined by Qz + Bt + Pl ± Ky ± Grt ± Sil mesocratic domains, alternated with Sil + Qz ± Pl ± Bt leucocratic layers; $S_{2(L-GHS)}$ is defined by Bt + Sil. Grt is rare and includes Qz + Bt + Wm + Ky at its rims. Ky in the matrix is replaced by Pl.
U-GHS	**14-08a**	Bt + Sil + Grt migmatite	Qz, Pl, Bt, Wm, Kfs, Grt, Sil	Ilm	Banded structure, defined by Bt + Sil + Qz ± Grt mm-thick mesocratic domanis alternating with Qz + Pl + Kfs ± Sil ± Grt pluri-mm leucocratic layers; $S_{m(U-GHS)}$ defined by Bt + Sil. Grt is peritectic with nanogranites. Mirmeckites and symplectites are common. Local occurrence of melt pseudomorphs. Wm flakes overgrow $S_{m(U-GHS)}$.

Table 2

Table 2. Mineral compositions for the studied metapelites

		Grt	Bt	Wm	Pl	St	Chl
LHS	15-19	→		→			
		XMg=0.03-0.07 XCa=0.19-0.09 XMn=0.16-0.02 XFe=0.63-0.81	XMg^{i}=0.39 Ti^{i}=0.03 $XMg^{\#}$=0.39-0.41 $Ti^{\#}$=0.10-0.11 XMg=0.40-0.42 Ti=0.06-0.11	$Si^{\#}$=3.09-3.10 $Na^{\#}$=0.12-0.20 Si=3.09-3.18 Na=0.14-0.20 Si*=3.10-3.11 Na*=0.10-0.13	XAn=0.21-0.23 XAn^{i}=0.18-0.22		XMg*=0.39-0.40
	14-27a	→			→		
		XMg=0.030-0.055 XCa=0.25-0.19 XMn=0.15-0.05 XFe=0.57-0.72	XMg=0.38-0.43 Ti=0.09-0.13	$Si^{\#}$=3.05-3.13 $Na^{\#}$=0.08-0.14 Si=3.05-3.17 Na=0.08-0.14	XAn=0.34-0.28		XMg^{i}=0.39 $XMg^{\#}$=0.41-0.44 XMg*=0.41-0.44
	14-28b	→				→	
		XMg=0.08-0.13 XCa=0.17-0.14 XMn=0.02-0.00 XFe=0.72-0.75	XMg=0.51-0.56 Ti=0.06-0.10	Si=3.08-3.20 Na=0.1-0.14		XMg=0.18-0.13	
LHS (RTS)	15-26b	→			→		
		XMg=0.09-0.14 XCa=0.2-0.14 XMn=0.09-0.03 XFe=0.64-0.70	XMg^{i}=0.57-0.59 Tii=0.09-0.10 XMg=0.50-0.52 Ti=0.10-0.13	Si=3.07-3.18 Na=0.15-0.19	XAn=0.30-0.24		XMg*=0.16
L-GHS	14-03	→			→		
		XMg=0.14-0.18 XCa=0.075-0.05 XMn=0.07-0.035 XFe=0.71-0.74	XMg^{i}=0.61-0.68 Ti^{i}=0.09-0.12 XMg=0.44-0.51 Ti=0.10-0.18	Si=3.09-3.14 Na=0.13-0.14	XAn=0.17-0.22		XMg*=0.24-0.51
	14-25b	→				→	
		XMg=0.13-0.15 XCa=0.04-0.03 XMn=0.05-0.035 XFe=0.78-0.81	XMg^{i}=0.44-0.54 Ti^{i}=0.10-0.14 XMg=0.38-0.46 Ti=0.09-0.17	Si=3.07-3.10 Na=0.15-0.17	XAn^{i}=0.12 XAn=0.15-0.16	XMg=0.16-0.12	
	15-38	→				→	
		XMg=0.09-0.14 XCa=0.08-0.04 XMn=0.11-0.03 XFe=0.72-0.80	XMg^{i}=0.51 Ti^{i}=0-0.11 XMg=0.48-0.50 Ti=0.09-0.17	Si*=3.03-3.09 Na*=0.15-0.22 Si=3.08-3.16 Na=0.15-0.22	XAn^{i}=0.30-0.32 XAn=0.16-0.24	XMg=0.20-0.16	XMg*=0.26-0.36
	14-24	→			→	→	
		XMg=0.14-0.16 XCa=0.05-0.04 XMn=0.05-0.04 XFe=0.75-0.79	XMg^{i}=0.50-0.55 Ti^{i}=0.13-0.16 XMg=0.41-0.47 Ti=0.10-0.24	Si=3.08-3.15 Na=0.13-0.14	XAn^{i}=0.23 XAn=0.15-0.22	XMg=0.16-0.14	

Table 2 *(continued).* Mineral compositions for the studied metapelites

		Grt	Bt	Wm	Pl	St	Chl
L-GHS	**14-44a**	XMg=0.16-0.18 XCa=0.04-0.05 XMn=0.05-0.06 XFe=0.72-0.75	XMg^{i}=0.57-0.60 Ti^{i}=0.11-0.15 XMg=0.45-0.49 Ti=0.16-0.19	→ Si=3.16-3.07 Na=0.09-0.12 Si*=3.07-3.12 Na*=0.10	→ XAn=0.18-0.26		XMg*=0.48
	14-61b	XMg=0.12-0.13 XCa=0.02-0.03 XMn=0.03-0.04 XFe=0.80-0.84	XMg^{i}=0.26-0.29 Ti^{i}=0.11-0.16 XMg=0.28-0.34 Ti=0.11-0.21	Si^{i}=3.11-3.15 Na^{i}=0.05-0.06 Si=3.07-3.11 Na=0.05-0.09	→ XAn^{i}=0.11-0.12 XAn=0.02-0.10		
	14-71	XMg=0.10-0.11 XCa=0.04-0.03 XMn=0.035-0.040 XFe=0.84-0.87	XMg^{i}=0.35-0.42 Ti^{i}=0.22-0.23 XMg=0.28-0.36 Ti=0.15-0.25	Si=3.06-3.10 Na=0.12-0.14	→ XAn^{i}=0.18-0.20 XAn=0.14		
	14-52	XMg=0.20-0.21 XCa=0.025-0.03 XMn=0.11-0.12 XFe=0.64-0.67	XMg^{i}=0.50 Ti=0.12 XMg=0.47-0.55 Ti=0.14-0.23	Si^{i}=3.08 Na^{i}=0.045	→ XAn=0.12-0.15		
U-GHS	**14-08a**	XMg=0.10-0.12 XCa=0.035-0.045 XMn=0.07-0.08 XFe=0.78-0.81	XMg^{i}=0.37-0.38 Ti^{i}=0.17 XMg=0.29-0.33 Ti=0.23-0.30	Si*=3.07-3.10 Na*=0.05-0.10	→ XAn^{i}=0.33 XAn=0.26-0.03		XMg*=0.19
	14-12	XMg=0.10-0.11 XCa=0.02 XMn=0.04-0.07 XFe=0.80-0.84	XMg^{i}=0.35-0.40 Ti^{i}=0.04-0.09 XMg=0.35-0.40 Ti=0.06-0.20	Si*=3.07-3.09 Na*=0.06-0.09	→ XAn^{i}=0.20-0.21 XAn=0.22-0.02		

The arrows indicate a zonation from core to rim; Ti, Si, Na are expressed as a.p.f.u.

^{i} included in garnet. * overgrowing Sm. ^{f} fibrolitic, replacing Grt and Wm at the rims $^{\#}$ defining S_{m-1}

Table 3 - Average pressure-temperatures estimates for the selected metapelites

	Sample	Assemblage	aH_2O	T (°C)	P (kbar)	N° of reactions
LHS	15-19*	Grt-Bt-Wm-Pl-Qz-H_2O	1	538±31	7.0±1.3	5
	15-19	Grt-Bt-Wm-Pl-Qz-H_2O	1	591±23	7.5±1.0	5
	14-27a*	Grt-Bt-Wm-Pl-Qz-H_2O	1	541±23	6.6±0.9	4
	14-27a	Grt-Bt-Wm-Pl-Qz-H_2O	1	603±28	8.2±1.4	5
	15-28b	Grt-Bt-Wm-St-Ky-Qz-H_2O	1	604±23	7.1±2.1	5
LHS (RTS)	15-26b*	Grt-Bt-Wm-Pl-Qz-H_2O	1	584±25	7.8±1.0	4
	15-26b	Grt-Bt-Wm-Pl-Qz-H_2O	1	607±24	8.8±1.0	4
L-GHS	14-03*	Grt-Bt-Wm-Pl-Qz-H_2O	1	632±22	7.0±1.0	5
	14-03	Grt-Bt-Wm-Pl-Qz-H_2O	1	673±31	8.7±1.3	5
			0.9	663±32	8.6±1.3	5
	14-25b*	Grt-Bt-Wm-Pl-Qz-H_2O	1	602±25	6.4±1.2	4
	14-25b	Grt-Bt-Wm-Pl-Ky-Qz-H_2O	1	660±37	8.3±2.1	6
			0.9	648±36	8.2±2.1	6
	15-38*	Grt-Bt-Wm-Pl-Qz-H_2O	1	640±20	7.2±0.7	7
	15-38	Grt-Bt-Wm-Pl-St-Ky-Qz-H_2O	1	678±17	8.7±1.0	9
			0.9	666±17	8.5±1.1	9
	14-24	Grt-Bt-Wm-Pl-Ky-Qz-H_2O	1	711±35	8.9±1.9	6
			0.9	699±34	8.8±1.9	6
	14-44a	Grt-Bt-Wm-Pl-Ky-Qz-H_2O	1	696±39	9.3±2.2	6
			0.9	676±34	8.9±1.9	6
	14-61b	Grt-Bt-Wm-Pl-Qz-H_2O	0.9	701±42	9.8±1.7	6
	14-71	Grt-Bt-Wm-Pl-Qz-H_2O	1	676±39	9.1±1.6	5
			0.9	662±55	8.3±2.3	5
	14-52	Grt-Bt-Wm-Pl-Ky-Qz-H_2O	1	850±68	11.3±2.6	7
			0.9	835±67	11.3±2.7	7
U-GHS	14-08a	Grt-Bt-Pl-Kfs-Sil-Qz-H_2O	0.7	816±86	5.9±2.0	4
	14-12	Grt-Bt-Pl-Kfs-Sil-Qz-H_2O	0.7	803±68	6.1±2.1	4

* refer to the prograde mineral assemblage

Table 4

Table 4a - Summary of the peak P-T constraints obtained from pseudosections (with errors) and T/P ratios

		Sample	average T (°C)	error (σ) T (°C)	weight T	average P (kbar)	error (σ) P (kbar)	weight P	average T/P (°C/kbar)	error (σ) T/P (°C/kbar)	weight T/P
Langtang-Gatlang	**U-GHS**	14-08	***780***	***20***		***7.8***	***0.8***		***101***	***12***	
	L-GHS	14-24	743	18	0.003	10.3	0.6	3.31	72	6	0.0320
		14-25b	720	5	0.040	9.9	0.2	44.44	73	1.6	0.3807
		14-03	720	10	0.010	10.3	0.7	2.04	70	6	0.0305
Gosainkund-Helambu	**L-GHS**	14-52	740	20	0.003	9.5	0.5	4.00	78	6	0.0260
		14-71	730	20	0.003	9.7	1.2	0.76	76	11	0.0081
		14-61b	740	10	0.010	10.4	1.0	1.11	71	8	0.0176
		14-44a	725	25	0.002	9.3	0.7	2.04	78	9	0.0137
		*weighted mean**	***725***	***4***		***9.9***	***0.1***		***73***	***1.4***	
	LHS-RTS	15-26b	***635***	***15***		***9.6***	***0.9***		***66***	***7***	
	LHS	14-27a	***595***	***25***		***7.5***	***0.8***		***80***	***11***	

Table 4b - Summary of the peak P-T constraints obtained from ''Average PT'' method (with errors) and T/P ratios

Langtang-Gatlang	**U-GHS**	14-12	803	68	0.0002	6.1	2.1	0.23	132	56	0.0003
		14-08a	816	86	0.0001	6.0	2.0	0.25	136	60	0.0003
		*weighted mean**	***808***	***53***		***6.0***	***1.4***		***134***	***41***	
	L-GHS	14-24	711	35	0.0008	8.9	1.9	0.28	80	21	0.0023
		14-25b	660	37	0.0007	8.3	2.1	0.23	80	25	0.0017
		15-38	678	17	0.0035	8.7	1.0	1.00	78	11	0.0084
		14-03	673	31	0.0010	8.7	1.3	0.59	77	15	0.0044
Gosainkund-Helambu	**L-GHS**	14-52	850	68	0.0002	11.3	2.6	0.15	75	23	0.0018
		14-71	676	39	0.0007	9.1	1.6	0.39	74	17	0.0033
		14-61b	701	42	0.0006	9.8	1.7	0.35	72	17	0.0036
		14-44a	696	39	0.0007	9.3	2.2	0.21	75	22	0.0021
		*weighted mean**	***687***	***11***		***9.0***	***0.6***		***76***	***6***	
	LHS-RTS	15-26b	***607***	***24***		***8.8***	***1.0***		***69***	***11***	
	LHS	15-28b	604	23	0.0019	7.1	2.1	0.23	85	28	0.0012
		14-27a	*596*	*24*	0.0017	*7.5*	*0.9*	1.23	79	13	0.0062
		15-19	591	23	0.0019	7.5	1.0	1.00	79	14	0.0054
		*weighted mean**	**597**	**13**		**7.5**	**0.6**		***80***	***9***	

*Where more than one sample are available, the weighted mean (with error) is calculated (i.e. values with smaller errors weight more than values with bigger errors).

Supplementary Material

Click here to download Supplementary Interactive Plot Data (CSV): Supplementary Material.docx

Graphical Abstract (for review)